

1 LEVERAGING MULTI-MESSENGER ASTROPHYSICS FOR DARK MATTER SEARCHES

By

Daniel Nicholas Salazar-Gallegos

A DISSERTATION

Submitted to
Michigan State University
in partial fulfillment of the requirements
for the degree of

Physics—Doctor of Philosophy
Computational Mathematics in Science and Engineering—Dual Major

Today

ABSTRACT

3 I did Dark Matter with HAWC and IceCube. I also used Graph Neural Networks

⁴ Copyright by

⁵ DANIEL NICHOLAS SALAZAR-GALLEGOS

⁶ Today

ACKNOWLEDGMENTS

8 I love my friends. Thanks to everyone that helped me figure this out. Amazing thanks to the people
9 at LANL who supported me. Eames, etc Dinner Parties Jenny and her child Kaydince Kirsten, Pat,
10 Andrea Family. You're so far but so critical to my formation. Unconditional love. Roommate

TABLE OF CONTENTS

12	LIST OF TABLES	vii
13	LIST OF FIGURES	viii
14	LIST OF ABBREVIATIONS	xiii
15	CHAPTER 1 INTRODUCTION	1
16	CHAPTER 2 DARK MATTER IN THE COSMOS	2
17	2.1 Introduction	2
18	2.2 Dark Matter Basics	3
19	2.3 Evidence for Dark Matter	4
20	2.4 Searching for Dark Matter: Particle DM	11
21	2.5 Sources for Indirect Dark Matter Searches	16
22	2.6 Multi-Messenger Dark Matter	18
23	CHAPTER 3 MULTIMESSENGER ASTROPHYSICS: DETECTING HIGH EN-	
24	ERGY NEUTRAL MESSENGERS	21
25	3.1 Introduction	21
26	3.2 Charged Particles in a Medium	21
27	3.3 Photons (γ)	22
28	3.4 Neutrinos (ν)	22
29	3.5 Opportunities to Combine for Dark Matter	22
30	CHAPTER 4 HIGH ALTITUDE WATER CHERENKOV (HAWC) OBSERVATORY .	24
31	4.1 The Detector	24
32	4.2 Events Reconstruction and Data Acquisition	24
33	4.3 Remote Monitoring	24
34	CHAPTER 5 ICECUBE NEUTRINO OBSERVATORY	25
35	5.1 The Detector	25
36	5.2 Events Reconstruction and Data Acquisition	25
37	5.3 Northern Test Site	25
38	CHAPTER 6 COMPUTATIONAL TECHNIQUES IN PARTICLE ASTROPHYSICS .	26
39	6.1 Neural Networks for Gamma/Hadron Separation	26
40	6.2 Parallel Computing for Dark Matter Analyses	26
41	CHAPTER 7 GLORY DUCK: MULTI-WAVELENGTH SEARCH FOR DARK MATT-	
42	TER ANNIHILATION TOWARDS DWARF SPHEROIDAL GALAX-	
43	IES	27
44	7.1 Introduction	27
45	7.2 Dataset and Background	29
46	7.3 Analysis	30

47	7.4 HAWC Results	38
48	7.5 Glory Duck Combined Results	39
49	7.6 HAWC Systematics	43
50	7.7 <i>J</i> -factor distributions	48
51	7.8 Discussion and Conclusions	53
52	CHAPTER 8 NU DUCK	57
53	CHAPTER 9 MULTITHREADING HAWC ANALYSES FOR DARK MATTER	
54	SEARCHES	58
55	APPENDIX A MULTI-EXPERIMENT SUPPLEMENTARY FIGURES	59
56	BIBLIOGRAPHY	61

LIST OF TABLES

<p>58 Table 7.1 Summary of the relevant properties of the dSphs used in the present work. 59 Column 1 lists the dSphs. Columns 2 and 3 present their heliocentric distance 60 and galactic coordinates, respectively. Columns 4 and 5 report the J-factors of 61 each source given from the \mathcal{GS} and \mathcal{B} independent studies and their estimated 62 $\pm 1\sigma$ uncertainties. The values $\log_{10} J$ (\mathcal{GS} set) [44] correspond to the mean 63 J-factor values for a source extension truncated at the outermost observed star. 64 The values $\log_{10} J$ (\mathcal{B} set) [46] are provided for a source extension at the tidal 65 radius of each dSph. Bolded sources are within HAWC's field of view and 66 provided to the Glory Duck analysis.</p>	<p style="margin-top: 100px;">. 35</p>
<p>67 Table 7.2 Summary of dSph observations by each experiment used in this work. A 68 ‘-’ indicates the experiment did not observe the dSph for this study. For 69 Fermi-LAT, the exposure at 1 GeV is given. For HAWC, $\Delta\theta$ is the absolute 70 difference between the source declination and HAWC latitude. HAWC is more 71 sensitive to sources with smaller $\Delta\theta$. For IACTs, we show the zenith angle 72 range, the total exposure, the energy range, the angular radius θ of the signal or 73 ON region, the ratio of exposures between the background-control (OFF) and 74 signal (ON) regions (τ), and the significance of gamma-ray excess in standard 75 deviations, σ.</p>	<p style="margin-top: 100px;">. 36</p>
<p>76 Proof I know how to include</p>	

LIST OF FIGURES

<p>78 Figure 2.1 Rotation curve fit to NGC 6503 from [7]. Dashed line is the contribution 79 from visible matter. Dotted curves are from gas. Dash-dot curves are from 80 dark matter (DM). Solid line is the composite contribution from all matter 81 and DM sources. Data are indicated with bold dots with error bars. Data 82 agree strongly with a matter + DM composite prediction.</p> <p>83 Figure 2.2 Light from distant galaxy is bent in unique ways depending on the distribution 84 of mass between the galaxy and Earth. Yellow dashed lines indicate where 85 the light would have gone if the matter were not present [8].</p> <p>86 Figure 2.3 (left) Optical image of galactic cluster 1E0657-558. (right) X-ray image of the 87 cluster with redder meaning hotter and higher baryon density. (both) Green 88 contours are reconstruction of gravity contours from weak lensing. White 89 rings are the best fit mass maxima at 68.3%, 95.5%, and 99.7% confidence. 90 The matter maxima of the clusters are clearly separated from x-ray maxima. [9]</p> <p>91 Figure 2.4 Plank CMB sky. Sky map features small variations in temperature in primor- 92 dial light. These anisotropies are used to make inferences about the universe's 93 energy budget and developmental history. [10]</p> <p>94 Figure 2.5 Observed Cosmic Microwave Background power spectrum as a function of 95 multipole moment from Plank [10]. Blue line is best fit model from ΛCDM. 96 Red points and lines are data and error, respectively.</p> <p>97 Figure 2.6 Predicted power spectra of CMB for different $\Omega_m h^2$ values for fixed baryon 98 density from [11]. (left) Low $\Omega_m h^2$ increases the prominence of first and 99 second peaks. (middle) $\Omega_m h^2$ is most similar to the observed power spectrum. 100 The second and third peaks are similar in height. (right) $\Omega_m h^2$ is large which 101 suppresses the first peak and raises the prominence of the third peak.</p> <p>102 Figure 2.7 The Standard Model (SM) of particle physics. Figure taken from http://www.quantumdiaries.org/2014/03/14/the-standard-model-a-beautiful-but-flawed-theory/</p> <p>103 </p> <p>104 </p> <p>105 Figure 2.8 Simplified Feynman diagram demonstrating with different ways DM can 106 interact with SM particles. The 'X's refer to the DM particles whereas the 107 SM refer to fundamental particles in the SM. The large circle in the center 108 indicates the vertex of interaction and is purposely left vague. The colored 109 arrows refer to different directions of time as well as their respective labels. 110 The arrows indicate the initial and final state of the DM -SM interaction in time.</p>	<p style="text-align: right;">5</p> <p style="text-align: right;">7</p> <p style="text-align: right;">8</p> <p style="text-align: right;">9</p> <p style="text-align: right;">10</p> <p style="text-align: right;">12</p> <p style="text-align: right;">13</p>
---	--

111	Figure 2.9 A single jet event in ATLAS detector from 2017 [16]. Jet momentum was 112 observed to be 1.9 TeV. Missing transverse momentum was observed to be 113 1.9 TeV compared to the initial transverse momentum of the event was 0. 114 Implied MET is traced by a red dashed line in event display.	14
115	Figure 2.10 More detailed pseudo-Feynman diagram of particle cascade from dark matter 116 annihilation into 2 quarks. The quarks hadronize and down to stable particles 117 like γ or the anti-proton (p^-). Diagram pulled from ICRC 2021 presentation 118 on DM annihilation search [17].	15
119	Figure 2.11 Dark Matter (DM) decay spectrum for $b\bar{b}$ initial state and γ final state. Redder 120 spectra are for larger DM masses. Bluer spectra are light DM masses. x is a 121 unitless factor defined as the ratio of the mass of DM, m_χ , and the final state 122 particle energy E_γ . Figure from [19].	17
123	Figure 2.12 Different dark matter density profiles compared. Some models produce ex- 124 ceptionally large densities at small r [20].	18
125	Figure 2.13 The Milky Way Galaxy in photons (γ) and neutrinos (ν) [22]. The Galactic 126 center is at $l=0^\circ$ and is the brightest region in all panels. (top) An Optical 127 color image of the Milky Way galaxy seen from Earth. Clouds of gas and dust 128 obscure some light from stars. (2nd down) Integrated flux of γ -rays observed 129 by the Fermi-LAT telescope [23]. (middle) Expected neutrino emission 130 that corresponds with Fermi-LAT observations. (2nd up) Expected neutrino 131 emission profile after considering detector systematics of IceCube. (bottom) 132 Observed neutrino emission from region of the galactic plane. Substantial 133 neutrino emission was detected.	19
134	Figure 2.14 Dark Matter annihilation spectra for different final state particle and standard 135 model annihilation channels [24]. Photons (red), e^\pm (green), \bar{p} (blue), ν (black).	20
136	Figure 3.1 TODO: Show a nuclear reactor with cherenkov radiation[NEEDS A SOURCE][FACT 137 CHECK THIS]	22
138	Figure 3.2 TODO: absorption spectrum of liquid and solid water[NEEDS A SOURCE][FACT 139 CHECK THIS]	23

140	Figure 7.1 [NEEDS A SOURCE] Sensitivities of five gamma-ray experiments compared 141 to percentages of the Crab nebula's emission and dark matter annihilation. 142 Solid lines present estimated sensitivities to power law spectra [FACT CHECK 143 THIS]for each experiment. Green lines are Fermi-LAT sensitivities where 144 lighter green is the sensitivity to the galactic center and dark green is its 145 sensitivity to higher declinations. Orange, red, and purple solid lines rep- 146 resent the MAGIC, HESS, and VERITAS 50 hour sensitivities respectively. 147 The maroon and brown lines are the HAWC 1 year and 5 year sensitivities. 148 Across four decades of gamma-ray energy, these experiments have similar 149 sensitivities on the order 10^{-12} erg cm $^{-2}$ s $^{-1}$. The dotted lines are estimated 150 dark matter fluxes assuming $m_\chi = 5$ TeV DM annihilating to bottom quarks 151 (red), tau leptons (blue), and W bosons (green). Faded gray lines outline 152 percentage flux of the Crab nebula.	28
153	Figure 7.2 Effect of Electro-Weak (EW) corrections on expected DM annihilation spec- 154 trum for $\chi\chi \rightarrow W^-W^+$. Solid lines are spectral models that consider EW 155 corrections. Dash-dot lines are spectral models without EW corrections. Red 156 lines are models for $M_\chi = 1$ TeV. Blue lines represent models for $M_\chi = 100$ 157 TeV. All models are sourced from the PPPC4DMID [43].	32
158	Figure 7.3 $\frac{dJ}{d\Omega}$ maps for Segue1 (top) and Coma Berenices (bottom). Origin is centered 159 on the specific dwarf spheroidal galaxies (dSph). X and Y axes are the 160 angular separation from the center of the dwarf. Plots of the remaining 11 161 dSph HAWC studied are linked in Fig. A.1.	34
162	Figure 7.4 Illustration of the combination technique showing a comparison between 163 $-2 \ln \lambda$ provided by four instruments (colored lines) from the observation 164 of the same dSph without any J nuisance and their sum, <i>i.e.</i> the result- 165 ing combined likelihood (thin black line). According to the test statistics 166 of Equation (7.10), the intersection of the likelihood profiles with the line 167 $-2 \ln \lambda = 2.71$ indicates the 95% C.L. upper limit on $\langle \sigma v \rangle$. The combined 168 likelihood (thin black line) shows a smaller value of upper limit on $\langle \sigma v \rangle$ 169 than those derived by individual instruments. We also show the uncertainties 170 on the J -factor affects the combined likelihood and degrade the upper limit 171 on $\langle \sigma v \rangle$ (thick black line). All likelihood profiles are normalized so that the 172 global minimum $\widehat{\langle \sigma v \rangle}$ is 0. We note that each profile depends on the observa- 173 tional conditions in which a target object was observed. The sensitivity of a 174 given instrument can be degraded and the upper limits less constraining if the 175 observations are performed in non optimal conditions such as a high zenith 176 angle or a short exposure time.	39
177	Figure 7.5 HAWC upper limits at 95% confidence level on $\langle \sigma v \rangle$ versus DM mass for 178 seven annihilation channels, using the set of J -factors from Ref. [47] The 179 solid line represents the observed combined limit. Dashed lines represent 180 limits from individual dSphs.	40

181	Figure 7.6 HAWC Brazil bands at 95% confidence level on $\langle\sigma v\rangle$ versus DM mass for	41
182	seven annihilation channels with J -factors from \mathcal{GS} [47]. The solid line	
183	represents the combined limit from 13 dSphs. The dashed line is the expected	
184	limit. The green band is the 68% containment. The yellow band is the 95%	
185	containment.	
186	Figure 7.7 Upper limits at 95% confidence level on $\langle\sigma v\rangle$ in function of the DM mass for	44
187	eight annihilation channels, using the set of J factors from Ref. [47] (\mathcal{GS} set	
188	in Table 7.1). The black solid line represents the observed combined limit,	
189	the black dashed line is the median of the null hypothesis corresponding	
190	to the expected limit, while the green and yellow bands show the 68% and	
191	95% containment bands. Combined upper limits for each individual detector	
192	are also indicated as solid, colored lines. The value of the thermal relic	
193	cross-section in function of the DM mass is given as the red dotted-dashed	
194	line [52].	
195	Figure 7.8 Same as Fig. 7.7, using the set of J factors from Ref. [46, 51] (\mathcal{B} set in Table 7.1).	45
196	Figure 7.9 Comparisons of the combined limits at 95% confidence level for each of the	46
197	eight annihilation channels when using the J factors from Ref. [47] (\mathcal{GS} set in	
198	Table 7.1), plain lines, and the J factor from Ref. [46, 51] (\mathcal{B} set in Table 7.1),	
199	dashed lines. The cross-section given by the thermal relic is also indicated [52].	
200	Figure 7.10 Comparisons of the combined limits at 95% confidence level for a point source	47
201	analysis and extended source using [47] \mathcal{GS} J-factor distributions and PPPC	
202	[43] annihilation spectra. Shown are the limits for Segue1 which will have	
203	the most significant impact on the combined limit. 6 of the 7 DM annihilation	
204	channels are shown. Solid lines are extended source studies. Dashed lines	
205	are point source studies. Overall, the extended source analysis improves the	
206	limit by a factor of 2.	
207	Figure 7.11 Same as Fig. 7.10 on Coma Berenices. This dSph also contributes signifi-	48
208	cantly to the limit. The limits are identical in this case.	
209	Figure 7.12 Comparison of combined limits when correcting for HAWC's pointing sys-	49
210	tematic. All DM annihilation channels are shown. The solid black line is the	
211	ratio between published limit to the declination corrected limit. The blue solid	
212	line or "Combined_og" represented the limits computed for Glory Duck. The	
213	solid orange line or "Combined_ad" represented the limits computed after	
214	correcting for the pointing systematic.	
215	Figure 7.13 Differential map of dJ/Ω from model built in Section 7.7.1 and profiles	51
216	provided directly from authors. (Top) Differential from Segue1. (bottom)	
217	Differential from Coma Berenices. Note that their scales are not the same.	
218	Segue1 shows the deepest discrepancies which is congruent with its large	
219	uncertainties. Both models show anuli where unique models become apparent.	

220	Figure 7.14 HAWC limits for Coma Berenices (top) and Segue1 (bottom) for two different 221 map sets. Blue lines are limits calculated on maps with poor model repre- 222 sentation. Orange lines are limits calculated on spatial profiles provided by 223 the authors of [44]. Black line is the ratio of the poor spatial model limits to 224 the corrected spatial models. The left y-axis measures $\langle\sigma v\rangle$ for the blue and 225 orange lines. The right y-axis measures the ratio and is unitless.	52
226	Figure 7.15 Comparisons between the J -factors versus the angular radius for the com- 227 putation of J factors from Ref. [47] (\mathcal{GS} set in Table 7.1) in blue and for 228 the computation from Ref. [46, 51] (\mathcal{B} set in Tab. 7.1) in orange. The solid 229 lines represent the central value of the J -factors while the shaded regions 230 correspond to the 1σ standard deviation.	54
231	Figure 7.16 Comparisons between the J -factors versus the angular radius for the computa- 232 tion of J factors from Ref. [47] (\mathcal{GS} set in Tab. 7.1) in blue and for the 233 computation from Ref. [46, 51] (\mathcal{B} set in Tab. 7.1) in orange. The solid 234 lines represent the central value of the J -factors while the shaded regions 235 correspond to the 1σ standard deviation.	55
236	Figure A.1 Sister figure to Figure 7.3. Sources in the first row from left to right: Boötes 237 I, Canes Venatici I, II. In second row: Draco, Hercules, Leo I. In the first row: 238 Leo II, Leo IV, Sextans. In the final row: Ursa Major I, Ursa Major II.	60

LIST OF ABBREVIATIONS

- 240 **MSU** Michigan State University
241 **LANL** Los Alamos National Laboratory
242 **DM** Dark Matter
243 **SM** Standard Model
244 **HAWC** High Altitude Water Cherenkov Observatory

245

CHAPTER 1

INTRODUCTION

246 Is the text not rendering right? Ah ok it knows im basically drafting the doc still

CHAPTER 2

247

DARK MATTER IN THE COSMOS

248 2.1 Introduction

249 The dark matter problem can be summarized in part by the following thought experiment.

250 Let us say you are the teacher for an elementary school classroom. You take them on a field
251 trip to your local science museum and among the exhibits is one for mass and weight. The exhibit
252 has a gigantic scale, and you come up with a fun problem for your class.

253 You ask your class, "What is the total weight of the classroom? Give your best estimation to
254 me in 30 minutes, and then we'll check your guess on the scale. If your guess is within 10% of the
255 right answer, we will stop for ice cream on the way back."

256 The students are ecstatic to hear this, and they get to work. The solution is some variation of
257 the following strategy. The students should give each other their weight or best guess if they do
258 not know. Then, all they must do is add each student's weight and get a grand total for the class.
259 The measurement on the giant scale should show the true weight of the class. When comparing
260 the measured weight to your estimation, multiply the measurement by 1.0 ± 0.1 to get the $\pm 10\%$
261 tolerances for your estimation.

262 Two of your students, Sandra and Mario, return to you with a solution.

263 They say, "We weren't sure of everyone's weight. We used 65 lbs. for the people we didn't
264 know and added everyone who does know. There are 30 of us, and we got 2,000 lbs.! That's a ton!"

265 You estimated 1,900 lbs. assuming the average weight of a student in your class was 60 lbs.
266 So, you are pleased with Sandra's and Mario's answer. You instruct your students to all gather on
267 the giant scale and read off the weight together. To all your surprise, the scale reads *10,000 lbs.*!
268 10,000 is significantly more than a 10% error from 2,000. In fact, it is approximately 5 times more
269 massive than either your or your students' estimates. You think to yourself and conclude there
270 must be something wrong with the scale. You ask an employee to check the scale and verify it is
271 well calibrated. They confirm that the scale is in working order. You weigh a couple of students
272 individually to assess that the scale is well calibrated. Sandra weighs 59 lbs., and Mario weighs

273 62 lbs., typical weights for their age. You then weigh each student individually and see that their
274 weights individually do not deviate greatly from 60 lbs. So, where does all the extra weight come
275 from?

276 This thought experiment serves as an analogy to the Dark Matter problem. The important
277 substitution to make however is to replace the students with stars and the classroom with a galaxy,
278 say the Milky Way. Individually the mass of stars is well measured and defined with the Sun as our
279 nearest test case. However, when we set out to measure the mass of a collection of stars as large as
280 galaxies, our well-motivated estimation is wildly incorrect. There simply is no way to account for
281 this discrepancy except without some unseen, or dark, contribution to mass and matter in galaxies.
282 I set out in my thesis to narrow the possibilities of what this Dark Matter could be.

283 This chapter is organized like the following... **TODO: Text should look like ... Chapter x has**
284 **blah blah blah.**

285 **2.2 Dark Matter Basics**

286 Presently, a more compelling theory of cosmology that includes Dark Matter (DM) in order
287 to explain a variety of observations is Λ Cold Dark Matter, or Λ CDM. I present the evidence
288 supporting Λ CDM in Section 2.3 yet discuss the conclusions of the Λ CDM model here. According
289 to Λ CDM fit to observations on the Cosmic Microwave Background (CMB), DM is 26.8% of the
290 universe's current energy budget. Baryonic matter, stuff like atoms, gas, and stars, contributes to
291 4.9% of the universe's current energy budget [1, 2, 3].

292 DM is dark; it does not interact readily with light at any wavelength. DM also does not interact
293 noticeably with the other standard model forces (Strong and Weak) at a rate that is readily observed
294 [3]. DM is cold, which is to say that the average velocity of DM is below relativistic speeds [1].
295 'Hot' DM would not likely manifest the dense structures we observe like galaxies, and instead
296 would produce much more diffuse galaxies than what is observed [3, 1]. DM is old; it played a
297 critical role in the formation of the universe and the structures within it [1, 2].

298 Observations of DM have so far been only gravitational. The parameter space available to what
299 DM could be therefore is extremely broad. The broad DM parameter space is iteratively tested in

300 DM searches by supposing a hypothesis that has not yet been ruled out and performing observations
301 to test them. When the observations yield a null result, the parameter space is constrained further.
302 I present some approaches for DM searches in Section 2.4.

303 **2.3 Evidence for Dark Matter**

304 Dark Matter (DM) has been a looming problem in physics for almost 100 years. Anomalies
305 have been observed by astrophysicists in galactic dynamics as early as 1933 when Fritz Zwicky
306 noticed unusually large velocity dispersion in the Coma cluster. Zwicky's measurement was the
307 first recorded to use the Virial theorem to measure the mass fraction of visible and invisible matter
308 in celestial bodies [4]. From Zwicky in [5], "*If this would be confirmed, we would get the surprising*
309 *result that dark matter is present in much greater amount than luminous matter.*" Zwicky's and
310 others' observation did not instigate a crisis in astrophysics because the measurements did not
311 entirely conflict with their understanding of galaxies [4]. In 1978, Rubin, Ford, and Norbert
312 measured rotation curves for ten spiral galaxies [6]. Rubin et al.'s 1978 publication presented a
313 major challenge to the conventional understanding of galaxies that could no longer be dismissed by
314 measurement uncertainties. Evidence has been mounting ever since for this exotic form of matter.
315 The following subsections provide three compelling pieces of evidence in support of the existence
316 of DM.

317 **2.3.1 First Clues: Stellar Velocities**

318 Zwicky, and later Rubin, measured the stellar velocities of various galaxies to estimate their
319 virial mass. The Virial Theorem upon which these observations are interpreted is written as

$$2T + V = 0. \quad (2.1)$$

320 Where T is the kinetic energy and V is the potential energy in a self-gravitating system. The
321 classical Newton's law of gravity from stars and gas was used for gravitational potential modeled in
322 the observed galaxies:

$$V = -\frac{1}{2} \sum_i \sum_{j \neq i} \frac{m_i m_j}{r_{ij}}. \quad (2.2)$$

323 Zwicky et al. measured just the velocities of stars apparent in optical wavelengths [5]. Rubin et al.
 324 added by measuring the velocity of the hydrogen gas via the 21 cm emission line of Hydrogen [6].
 325 The velocities of the stars and gas are used to infer the total mass of galaxies and galaxy clusters
 326 via Equation (2.1). An inferred mass is obtained from the luminosity of the selected sources. The
 327 two inferences are compared to each other as a luminosity to mass ratio which typically yielded [1]

$$\frac{M}{L} \sim 400 \frac{M_{\odot}}{L_{\odot}} \quad (2.3)$$

328 M_{\odot} and L_{\odot} referring to stellar mass and stellar luminosity, respectively. These ratios clearly indicate
 329 a discrepancy in apparent light and mass from stars and gas and their velocities.

330 Rubin et al. [6] demonstrated that the discrepancy was unlikely to be an underestimation of
 331 the mass of the stars and gas. The inferred "dark" mass was up to 5 times more than the luminous
 332 mass. This dark mass also needed to extend well beyond the extent of the luminous matter.

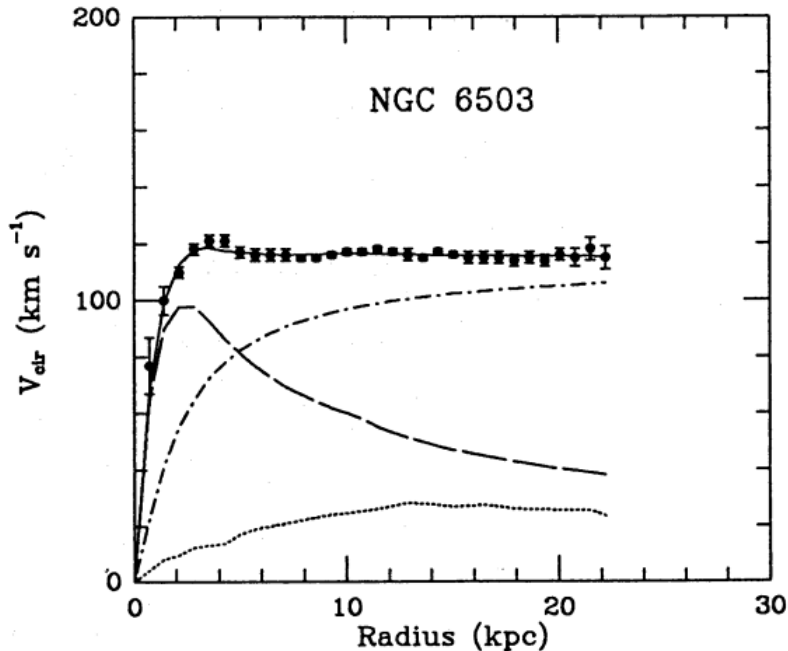


Figure 2.1 Rotation curve fit to NGC 6503 from [7]. Dashed line is the contribution from visible matter. Dotted curves are from gas. Dash-dot curves are from dark matter (DM). Solid line is the composite contribution from all matter and DM sources. Data are indicated with bold dots with error bars. Data agree strongly with a matter + DM composite prediction.

333 Figure 2.1 features one of many rotation curves plotted from the stellar velocities within galaxies.

334 The measured rotation curves mostly feature a flattening of velocities at higher radius which is not
335 expected if the gravity was only coming from gas and luminous matter. The extension of the
336 flat velocity region also indicates that the DM is distributed far from the center of the galaxy.
337 Modern velocity measurements include significantly larger objects, galactic clusters, and smaller
338 objects, dwarf galaxies. Yet, measurements along this regime are leveraging the Virial theorem
339 with Newtonian potential energies. We know Newtonian gravity is not a comprehensive description
340 of gravity. New observational techniques have been developed since 1978, and those are discussed
341 in the following sections.

342 **2.3.2 Evidence for Dark Matter: Gravitational Lensing**

343 Modern evidence for dark matter comes from new avenues beyond stellar velocities. Grav-
344 itational lensing from DM is a new channel from general relativity. General relativity predicts
345 aberrations in light caused by massive objects. In recent decades we have been able to measure the
346 lensing effects from compact objects and DM halos. Figure 2.2 shows how different massive ob-
347 jects change the final image of a faraway galaxy resulting from gravitational lensing. Gravitational
348 lensing developed our understanding of dark matter in two important ways.

349 Gravitational lensing provides additional compelling evidence for DM. The observation of two
350 merging galactic clusters in 2006, shown in Figure 2.3, provided a compelling argument for DM
351 outside the Standard Model. These clusters merged recently in astrophysical time scales. Galaxies
352 and star cluster have mostly passed by each other as the likelihood of their collision is low. Therefore,
353 these massive objects will mostly track the highest mass, dark and/or baryonic, density. Yet, the
354 intergalactic gas is responsible for the majority of the baryonic mass in the systems [4]. These gas
355 bodies will not phase through and will heat up as they collide together. The hot gas is located via
356 x-ray emission from the cluster. Two observations of the clusters were performed independently of
357 each other.

358 The first was the lensing of light around the galaxies due to their gravitational influences.
359 When celestial bodies are large enough, the gravity they exert bends space and time itself. The
360 warped space-time lenses light and will deflect in an analogous way to how glass lenses will bend

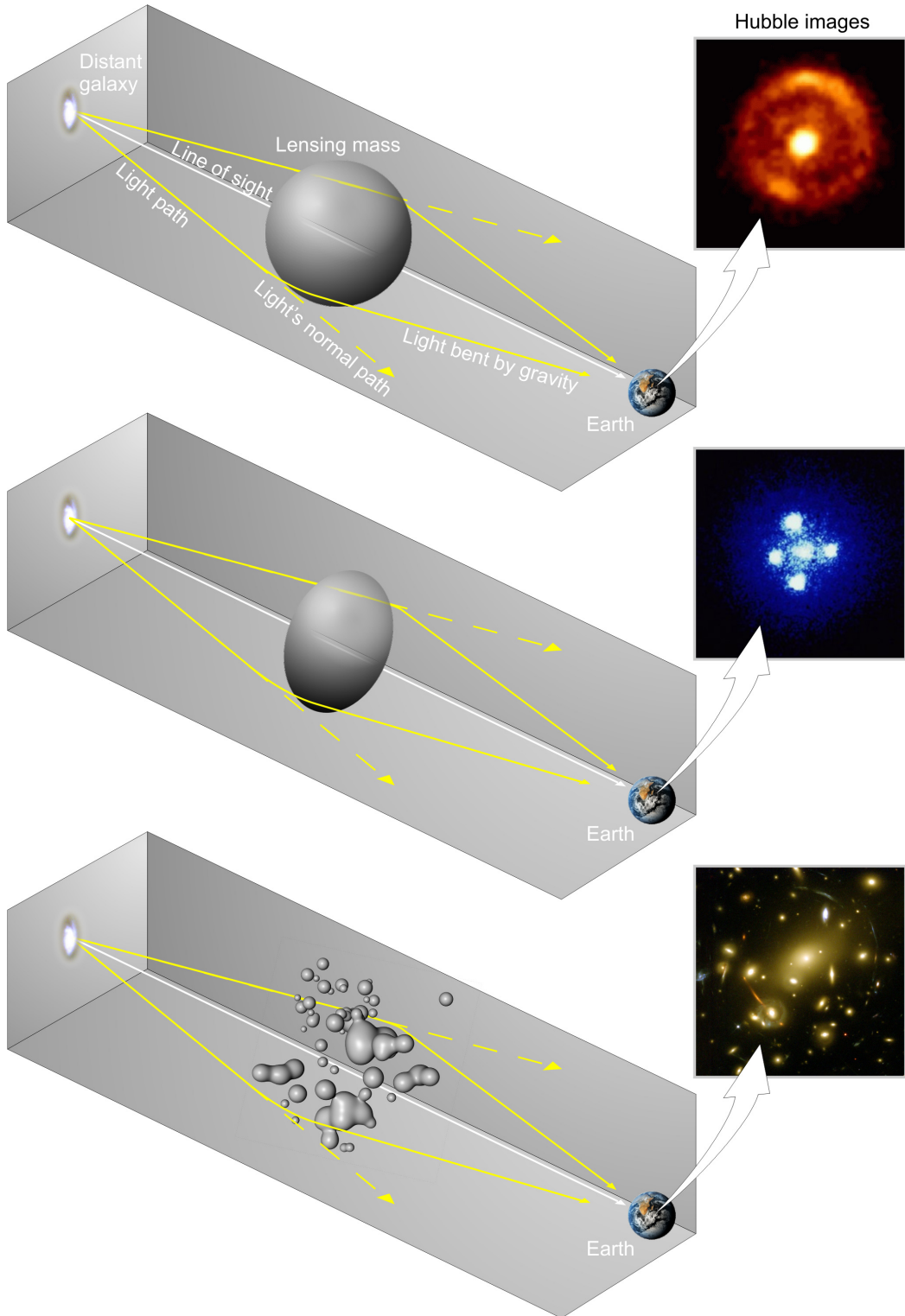


Figure 2.2 Light from distant galaxy is bent in unique ways depending on the distribution of mass between the galaxy and Earth. Yellow dashed lines indicate where the light would have gone if the matter were not present [8].

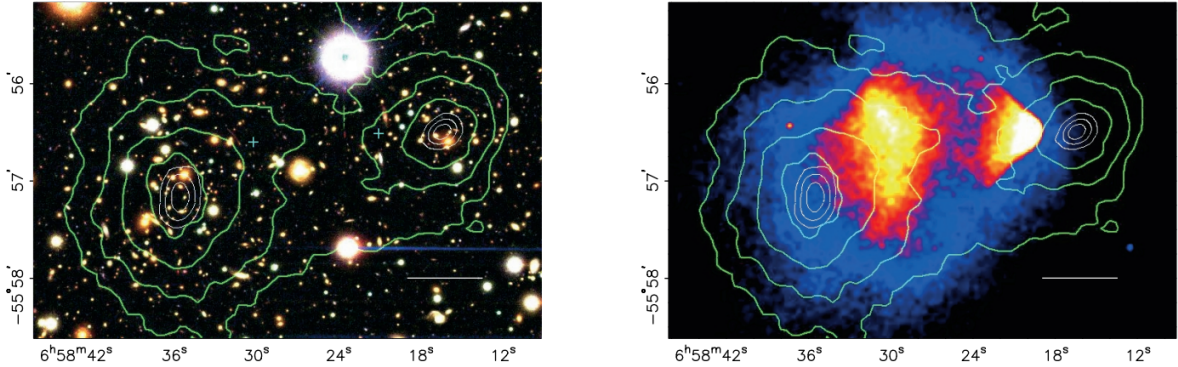


Figure 2.3 (left) Optical image of galactic cluster 1E0657-558. (right) X-ray image of the cluster with redder meaning hotter and higher baryon density. (both) Green contours are reconstruction of gravity contours from weak lensing. White rings are the best fit mass maxima at 68.3%, 95.5%, and 99.7% confidence. The matter maxima of the clusters are clearly separated from x-ray maxima. [9]

361 light, see Figure 2.2. With a sufficient understanding of light sources behind a massive object, we
 362 can reconstruct the contours of the gravitational lenses. The gradient of the contours shown in
 363 Figure 2.3 then indicates how dense the matter is and where it is.

364 The x-ray emission can then be observed from the clusters. Since these galaxies are mostly gas
 365 and are merging, then the gas should be getting hotter. If they are merging, the x-ray emissions
 366 should be the strongest where the gas is mostly moving through each other. Hence, X-ray emission
 367 maps out where the gas is in the merging galaxy cluster.

368 The lensing and x-ray observations were done on the Bullet cluster featured on Figure 2.3.
 369 The x-ray emissions do not align with the gravitational contours from lensing. The incongruence
 370 in mass density and baryon density suggests that there is a lot of matter somewhere that does
 371 not interact with light. Moreover, this dark matter cannot be baryonic [9]. The Bullet Cluster
 372 measurement did not really tell us what DM is exactly, but it did give the clue that DM also does
 373 not interact with itself very strongly. If DM did interact strongly with itself, then it would have been
 374 more aligned with the x-ray emission [9]. There have been follow-up studies of galaxy clusters with
 375 similar results. The Bullet Cluster and others like it provide a persuasive case against something
 376 possibly amiss in our gravitational theories.

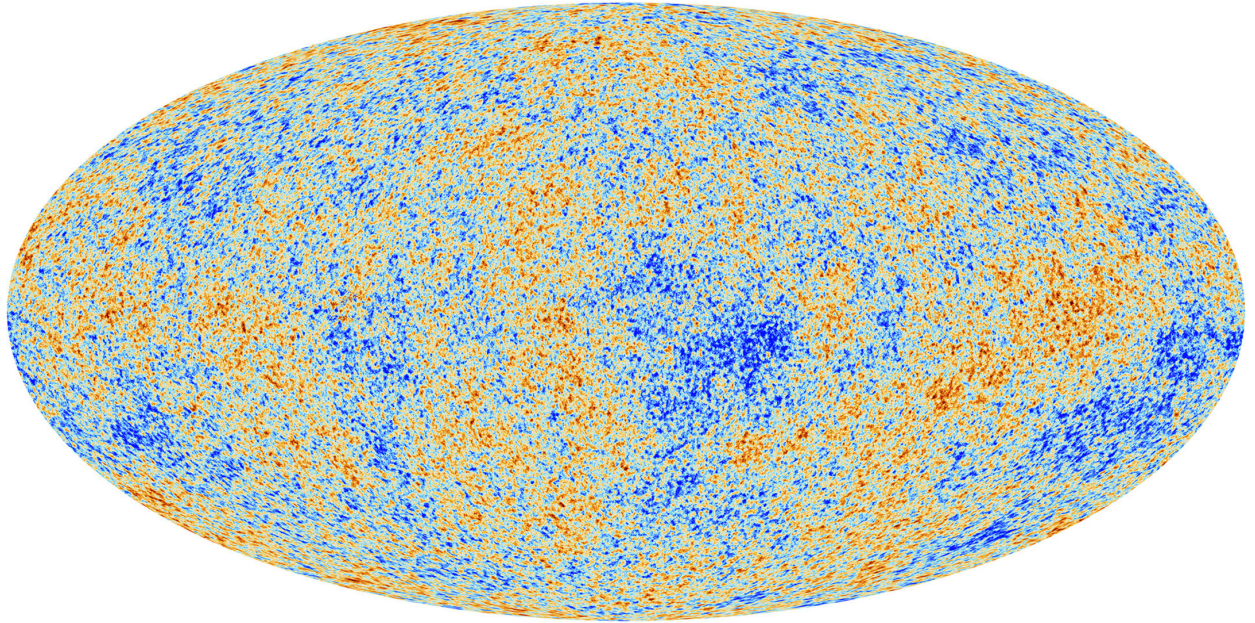


Figure 2.4 Plank CMB sky. Sky map features small variations in temperature in primordial light. These anisotropies are used to make inferences about the universe’s energy budget and developmental history. [10]

377 **2.3.3 Evidence for Dark Matter: Cosmic Microwave Background**

378 The Cosmic Microwave Background (CMB) is the primordial light from the early universe
379 when Hydrogen atoms formed from the free electron and proton soup in the early universe. The
380 CMB is the earliest light we can observe; released when the universe was about 380,000 years old.
381 Then we look at how the simulated universes look like compared to what we see. Figure 2.4 is the
382 most recent CMB image from the Plank satellite after subtracting the average value and masking the
383 galactic plane [10]. Redder regions indicate a slightly hotter region in the CMB, and blue indicates
384 colder. The intensity variations are on the order of 1 in 1000 with respect to the average value.

385 The Cosmic Microwave Background shows that the universe had DM in it from an incredibly
386 early stage. To measure the DM, Dark Energy, and matter fractions of the universe from the CMB,
387 the image is analyzed into a power spectrum, which shows the amplitude of the fluctuations as
388 a function of spherical multipole moments. Λ CDM provides the best fit to the power spectra of
389 the CMB as shown in Figure 2.5. The CMB power spectrum is quite sensitive to the fraction
390 of each energy contribution in the early universe. Low l modes are dominated by variations
391 in gravitational potential. Intermediate l emerge from oscillations in photon-baryon fluid from

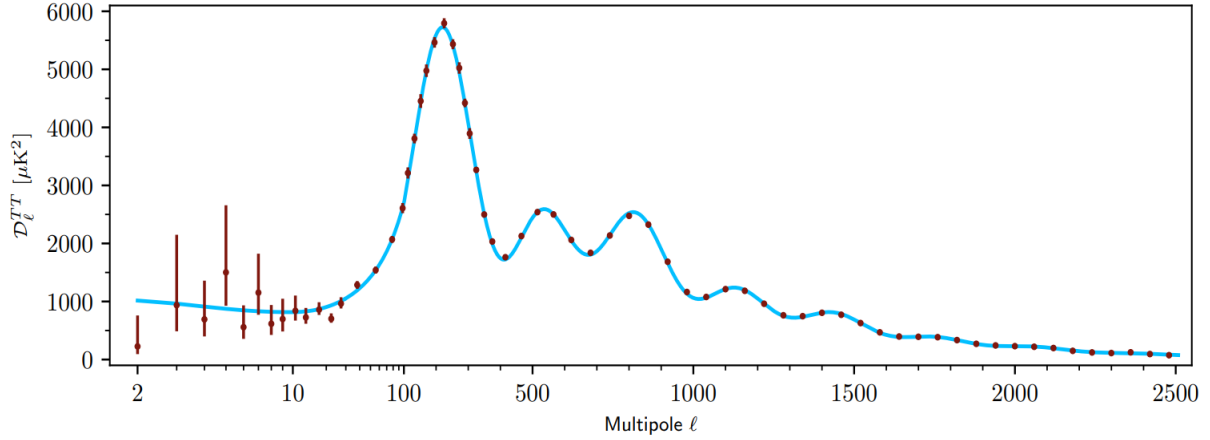


Figure 2.5 Observed Cosmic Microwave Background power spectrum as a function of multipole moment from Plank [10]. Blue line is best fit model from Λ CDM. Red points and lines are data and error, respectively.

392 competing baryon pressures and gravity. High l is a damped region from the diffusion of photons
 393 during electron-proton recombination. [1]

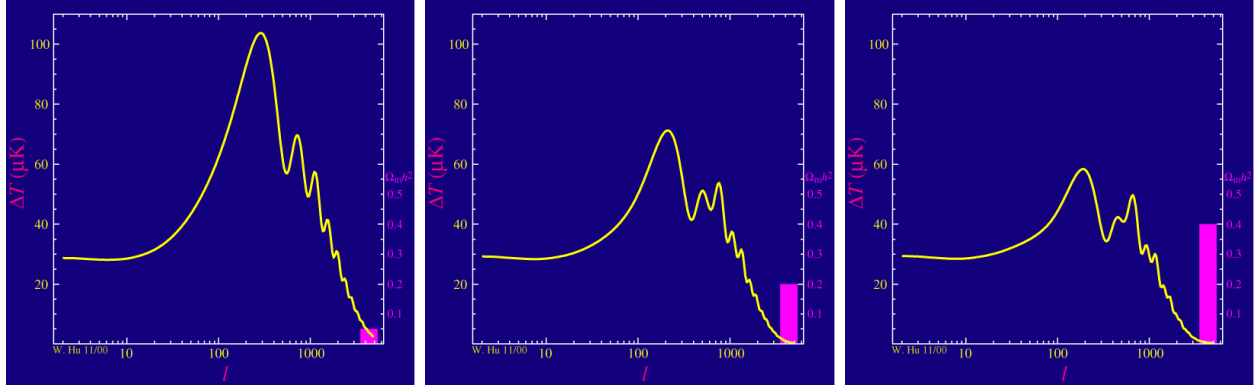


Figure 2.6 Predicted power spectra of CMB for different $\Omega_m h^2$ values for fixed baryon density from [11]. (left) Low $\Omega_m h^2$ increases the prominence of first and second peaks. (middle) $\Omega_m h^2$ is most similar to the observed power spectrum. The second and third peaks are similar in height. (right) $\Omega_m h^2$ is large which suppresses the first peak and raises the prominence of the third peak.

394 The harmonics would look quite different for a universe with less DM. Figure 2.6 demonstrates
 395 the effect $\Omega_m h^2$ has on the expected power spectrum for fixed baryon matter density. [11] Sweeping
 396 $\Omega_m h^2$ in this way clearly shows the effect dark matter has on the CMB power spectrum. The
 397 observations fit well with the Λ CDM model, and the derived fractions are as follows. The matter
 398 fraction: $\Omega_m = 0.3153$; and the baryon fraction: $\Omega_b = 0.04936$ [10]. Plank's observations also
 399 provide a measure of the Hubble constant, H_0 . H_0 especially has seen a growing tension in the

400 past decade that continues to deepened with observations from instruments like the James Webb
401 Telescope [12, 13]. As Hubble tensions deepen, we may find that perhaps Λ **CDM**, despite its
402 successes, is missing some critical physics.

403 Overall, the Newtonian motion of stars in galaxies, weak lensing from galactic clusters, and
404 power spectra from primordial light form a compelling body of research in favor of dark matter.
405 It takes another leap of theory and experimentation to make observations of DM that are non-
406 gravitational in nature. In Section 2.3, the evidence for DM implies strongly that the DM is matter
407 and not a lost parameter in the gravitational fields between massive objects. Finally, if we take one
408 axiom: that this matter has quantum behavior, such as being described by some Bohr wavelength
409 and abiding by some fermion or boson statistics; then we arrive at particle dark matter. One particle
410 DM hypothesis is the Weakly Interacting Massive Particle (WIMP). This DM candidate theory is
411 discussed further in the next section and is the focus of this thesis.

412 2.4 Searching for Dark Matter: Particle DM

413 Section 2.4 shows the Standard Model of particle physics and is currently the most accurate
414 model for the dynamics of fundamental particles like electrons and photons. The current status
415 of the SM does not have a viable DM candidate. When looking at the standard model, we can
416 immediately exclude any charged particle because charged particles interact strongly with light.
417 Specifically, this will rule out the following charged, fundamental particles: $e, \mu, \tau, W, u, d, s, c, t, b$
418 and their corresponding antiparticles. Recalling from Section 2.2 that DM must be long-lived and
419 stable over the age of the universe which excludes all SM particles with decay half-lives at or shorter
420 than the age of the universe. The lifetime constraint additionally eliminates the Z and H bosons.
421 Finally, the candidate DM needs to be somewhat massive. Recall from Section 2.2 that DM is cold
422 or not relativistic through the universe. This eliminates the remaining SM particles: $\nu_{e,\mu,\tau}, g, \gamma$ as
423 DM candidates. Because there are no DM candidates within the SM, the DM problem strongly
424 hints to physics beyond the SM (BSM).

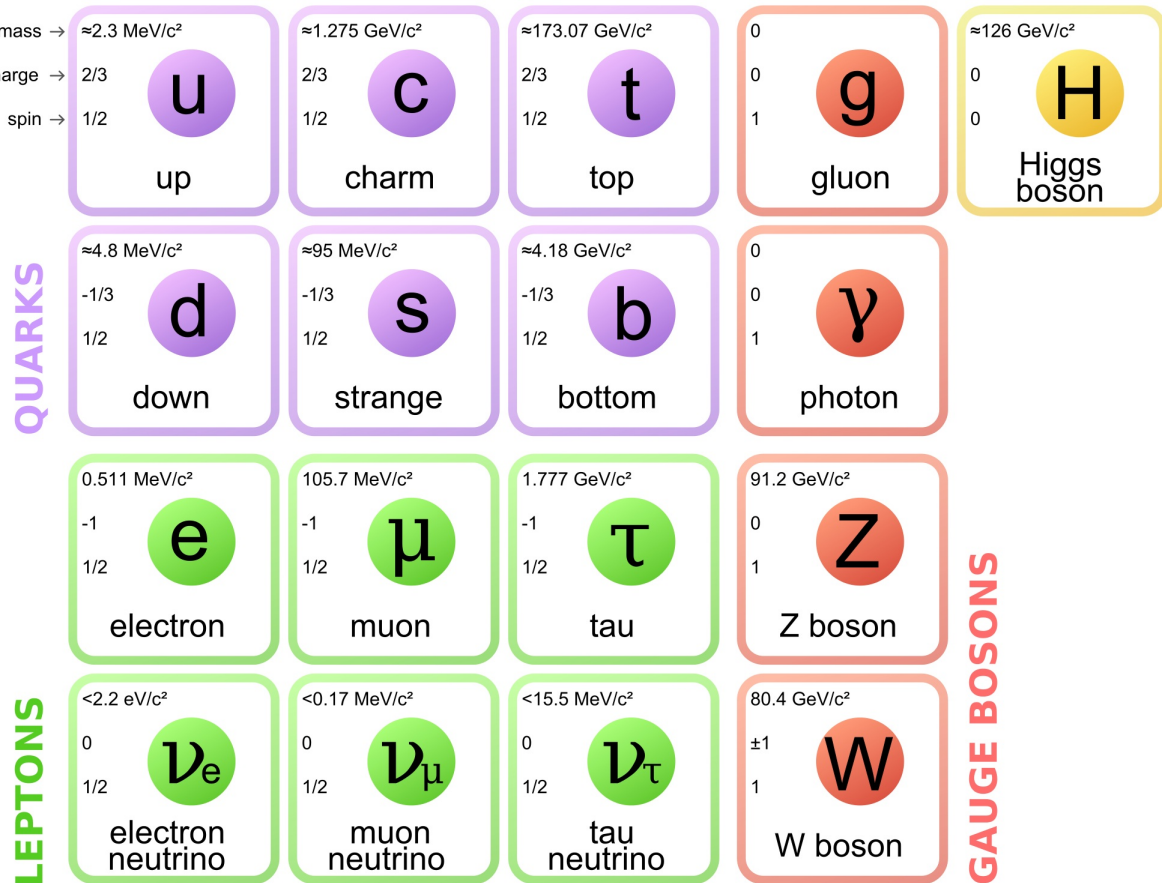


Figure 2.7 The Standard Model (SM) of particle physics. Figure taken from <http://www.quantumdiaries.org/2014/03/14/the-standard-model-a-beautiful-but-flawed-theory/>

425 2.4.1 Shake it, Break it, Make it

426 When considering DM that couples in some way with the SM, the interactions are roughly
 427 demonstrated by interaction demonstrated in Figure 2.8. The figure is a simplified Feynman
 428 diagram where the arrow of time represents the interaction modes of: **Shake it, Break it, Make it**.

429 **Shake it** refers to the direct detection of dark matter. Direct detection interactions start with
 430 a free DM particle and an SM particle. The DM and SM interact via elastic or inelastic collision
 431 and recoil away from each other. The DM remains in the dark sector and imparts some momentum
 432 onto the SM particle. The hope is that the momentum imparted onto the SM particle is sufficiently
 433 high enough to pick up with extremely sensitive instruments. Because we cannot create the DM in
 434 the lab, a direct detection experiment must wait until DM is incident on the detector. Most direct
 435 detection experiments are therefore placed in low-background environments with inert detection

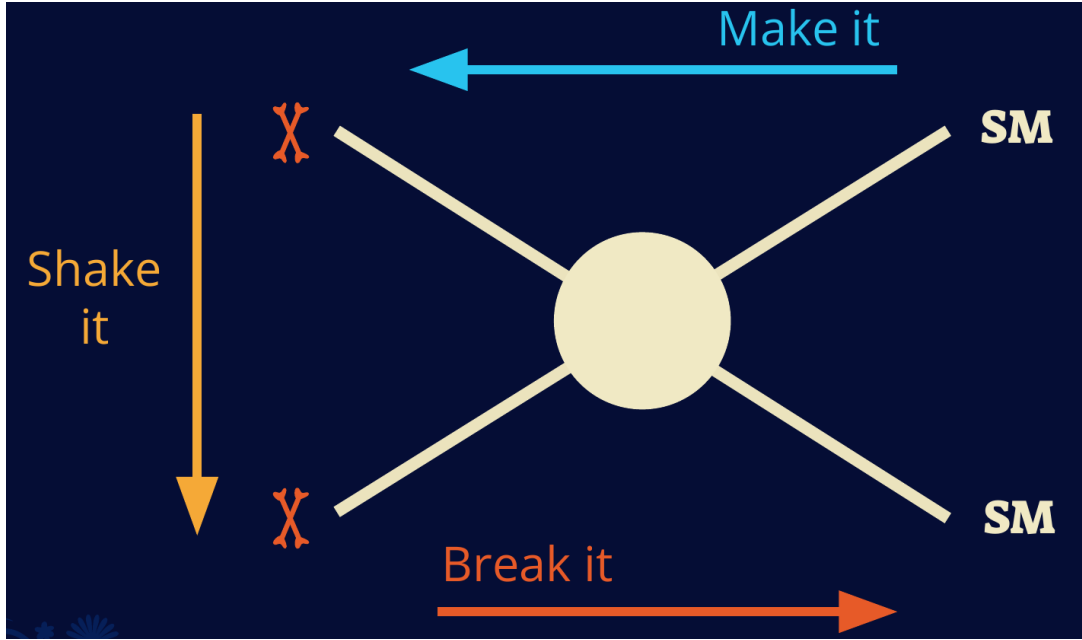


Figure 2.8 Simplified Feynman diagram demonstrating different ways DM can interact with SM particles. The 'X's refer to the DM particles whereas the SM refer to fundamental particles in the SM. The large circle in the center indicates the vertex of interaction and is purposely left vague. The colored arrows refer to different directions of time as well as their respective labels. The arrows indicate the initial and final state of the DM -SM interaction in time.

⁴³⁶ media like the noble gas Xenon. [14]

⁴³⁷ **Make it** refers to the production of DM from SM initial states. The experiment starts with
⁴³⁸ particles in the SM. These SM particles are accelerated to incredibly high energies and then collide
⁴³⁹ with each other. In the confluence of energy, DM hopefully emerges as a byproduct of the SM
⁴⁴⁰ annihilation. Often it is the collider experiments that are energetic enough to hypothetically produce
⁴⁴¹ DM. These experiments include the world-wide collaborations ATLAS and CMS at CERN where
⁴⁴² proton collide together at extreme energies. The DM searches, however, are complex. DM likely
⁴⁴³ does not interact with the detectors and lives long enough to escape the detection apparatus of
⁴⁴⁴ CERN's colliders. This means any DM production experiment searches for an excess of events
⁴⁴⁵ with missing momentum or energy in the events. An example event with missing transverse
⁴⁴⁶ momentum is shown in Figure 2.9. The missing momentum with no particle tracks implies a
⁴⁴⁷ neutral particle carried the energy out of the detector. However, there are other neutral particles
⁴⁴⁸ in the SM, like neutrons or neutrinos, so any analysis has to account for SM signatures of missing

449 momentum. [15]

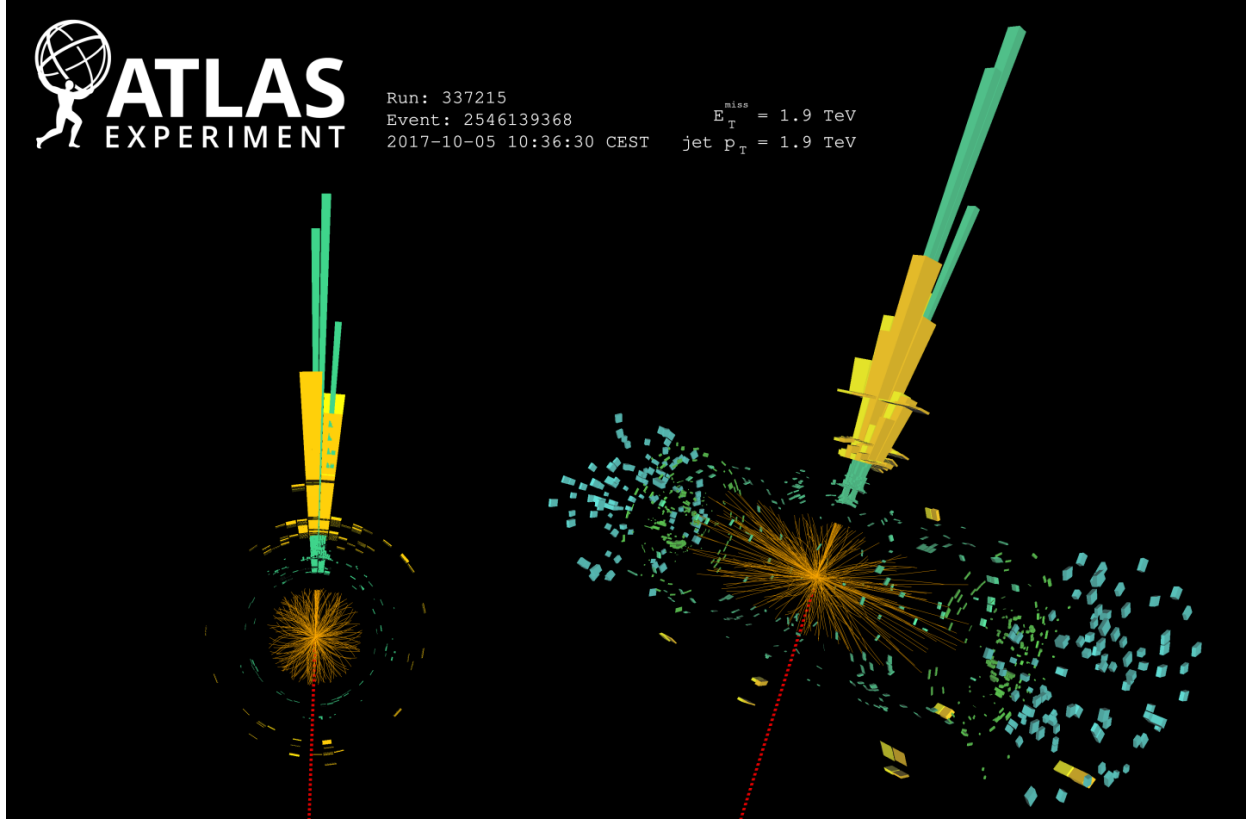


Figure 2.9 A single jet event in ATLAS detector from 2017 [16]. Jet momentum was observed to be 1.9 TeV. Missing transverse momentum was observed to be 1.9 TeV compared to the initial transverse momentum of the event was 0. Implied MET is traced by a red dashed line in event display.

450 2.4.2 Break it: Standard Model Signatures of Dark Matter through Indirect Searches

451 **Break it** refers to the creation of SM particles from the dark sector, and it is the primary focus
452 of this thesis. The interaction begins with DM or in the dark sector. The hypothesis is that this
453 DM will either annihilate with itself or decay and produce an SM byproduct. This method is
454 often referred to as the Indirect Detection of DM because we have no lab to directly control or
455 manipulate the DM. Therefore, most indirect DM searches are performed using observations of
456 known DM densities among the astrophysical sources. The strength is that we have the whole of the
457 universe and its 13.6-billion-year lifespan to use as a detector and particle accelerator. Additionally,
458 locations of dark matter are well cataloged since it was astrophysical observations that presented

459 the problem of DM in the first place.

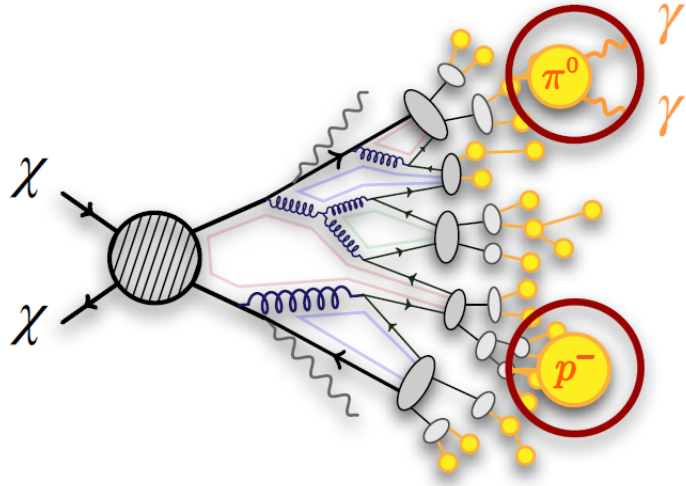


Figure 2.10 More detailed pseudo-Feynman diagram of particle cascade from dark matter annihilation into 2 quarks. The quarks hadronize and down to stable particles like γ or the anti-proton (p^-). Diagram pulled from ICRC 2021 presentation on DM annihilation search [17].

460 However, anything can happen in the universe. There are many difficult to deconvolve back-
461 grounds when searching for DM. One prominent example is the galactic center. We know the
462 galactic center has a large DM content because of stellar kinematics in our Milky Way and DM halo
463 simulations. Yet, any signal from the galactic center is challenging to parse apart from the extreme
464 environment of our supermassive black hole, unresolved sources, and diffuse emission from the
465 interstellar medium [18]. Despite the challenges, any DM model that yields evidence in the other
466 two observation methods, **Shake it or Make it** must be corroborated with indirect observations of
467 the known DM sources. Without corroborating evidence, DM observation in the lab is hard-pressed
468 to demonstrate that it is the model contributing to the DM seen at the universal scale.

469 In the case of WIMP DM, signals are described in terms of primary SM particles produced
470 from DM decay or annihilation. The SM initial state particles are then simulated down to stable
471 final states such as the γ , ν , p , or e which can traverse galactic lengths to reach Earth.

472 Figure 2.10 shows the quagmire of SM particles that emerges from SM initial states that are not
473 stable [17]. There are many SM particles with varying energies that can be produced in such an

474 interaction. For any arbitrary DM source and stable SM particle, the SM flux from DM annihilating
 475 to a neutral particle in the SM, ϕ , from a region in the sky is described by the following.

$$\frac{d\Phi_\phi}{dE_\phi} = \frac{\langle\sigma v\rangle}{8\pi m_\chi^2} \frac{dN_\phi}{dE_\phi} \times \int_{\text{source}} d\Omega \int_{l.o.s} \rho_\chi^2 dl(r, \theta') \quad (2.4)$$

476 In Equation (7.1), $\langle\sigma v\rangle$ is the velocity-weighted annihilation cross-section of DM to the SM. m_χ
 477 refers to the mass of DM, noted with Greek letter χ . $\frac{dN_\phi}{dE_\phi}$ is the N particle flux weighted by the
 478 particle energy. An example is provided in Figure 2.11 for the γ final state. The integrated terms
 479 are performed over the solid angle, $d\Omega$, and line of sight, l.o.s. ρ is the density of DM for a
 480 location (r, θ') in the sky. The terms left of the ' \times ' are often referred to as the particle physics
 481 component. The terms on the right are referred to as the astrophysical component. For decaying
 482 DM, the equation changes to...

$$\frac{d\Phi_\phi}{dE_\phi} = \frac{1}{4\pi\tau m_\chi} \frac{dN_\phi}{dE_\phi} \times \int_{\text{source}} d\Omega \int_{l.o.s} \rho_\chi dl(r, \theta') \quad (2.5)$$

483 In Equation (2.5), τ is the decay lifetime of the DM. Just as in Equation (7.1), the left and
 484 right terms are the particle physics and the astrophysical components respectively. The integrated
 485 astrophysical component of Equation (7.1) is often called the J-Factor. Whereas the integrated
 486 astrophysical component of Equation (2.5) is often called the D-Factor.

487 Exact DM $\text{DM} \rightarrow \text{SM SM}$ branching ratios are not known, so it is usually assumed to go 100%
 488 into an SM particle/anti-particle. Additionally, when a DM annihilation or decay produces one of
 489 the neutral, long-lived SM particles (ν or γ), the particle is traced back to a DM source. For DM
 490 above GeV energies, there are very few SM processes that can produce particles with such a high
 491 energy. Seeing such a signal would almost certainly be an indication of the presence of dark matter.
 492 Fortunately, the universe provides us with the largest volume and lifetime ever for a particle physics
 493 experiment.

494 2.5 Sources for Indirect Dark Matter Searches

495 The first detection of DM relied on optical observations. Since then, we have developed new
 496 techniques to find DM dense regions. As described in Section 2.3.1, many DM dense regions were
 497 through observing galactic rotation curves. Our Milky Way galaxy is among DM dense regions

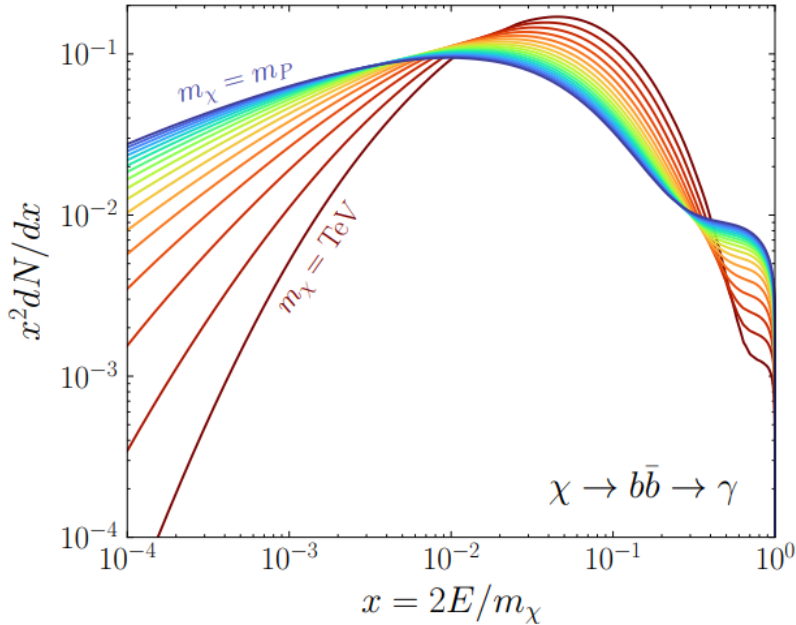


Figure 2.11 Dark Matter (DM) decay spectrum for $b\bar{b}$ initial state and γ final state. Redder spectra are for larger DM masses. Bluer spectra are light DM masses. x is a unitless factor defined as the ratio of the mass of DM, m_χ , and the final state particle energy E_γ . Figure from [19].

498 discovered, and it is the largest nearby DM dense region to look at. Additionally, the DM halo
 499 surrounding the Milky Way is clumpy [18]. There are regions in the DM halo of the Milky Way that
 500 have more DM than others that have captured gas over time. These sub-halos were dense enough
 501 collapse gas and form stars. These apparent sub galaxies are known as dwarf spheroidal galaxies
 502 and are the main sources studied in this thesis. Each source type comes with different trade-offs.
 503 Galactic Center studies will be very sensitive to the assumed distribution of DM. The central DM
 504 density can vary substantially as demonstrated in Figure 2.12. At distances close to the center of
 505 the galaxy, or small r , the differences in DM densities can be 3-4 orders of magnitude. Searches
 506 toward the galactic center will therefore be quite sensitive to the assumed DM distribution.

507 Searches toward Dwarf Spheroidal Galaxies (dSph's) suffer from uncertainties in the DM
 508 density less than the galactic center studies. This is mostly from their diminutive size being smaller
 509 than the angular resolution of most γ -ray observatories [18]. The DM content dSph's are typically
 510 determined with the Virial theorem, Equation (2.1), and are usually majority DM [18] in mass.
 511 Dsph's tend to be ideal sources to look at for DM searches. Their environments are quiet with little

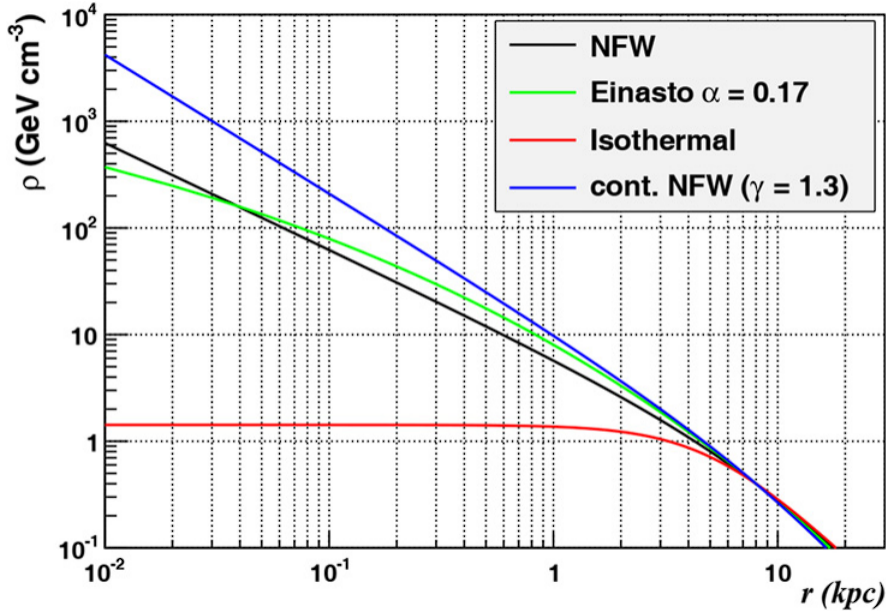


Figure 2.12 Different dark matter density profiles compared. Some models produce exceptionally large densities at small r [20].

512 astrophysical background. Unlike the galactic center, the most active components of dSph's are the
 513 stars within them versus a violent accretion disc around a black hole. All this together means that
 514 dSph's are among the best sources to look at for indirect DM searches. dSph's are the targets of
 515 focus for this thesis.

516 2.6 Multi-Messenger Dark Matter

517 Astrophysics entered a new phase in the past few decades that leverages our increasing sensitivity
 518 to SM channels and general relativity (GR). Up until the 21st century, astrophysical observations
 519 were performed with photons (γ) only. Astrophysics with this 'messenger' is fairly mature now.
 520 Novel observations of the universe have since only adjusted the sensitivity of the wavelength of
 521 light that is observed except at MeV energies. Gems like the CMB [10], and more have ultimately
 522 been observations of different wavelengths of light. Multi-messenger astrophysics proposes using
 523 other SM particles such the $p^{+/-}$, or ν or gravitation waves predicted by general relativity.

524 The experiment LIGO had a revolutionary discovery in 2016 with the first detection of a binary
 525 black hole merger [21]. This opened the collective imagination to observing the universe through
 526 gravitational waves. There has also been a surge of interest in the neutrino (ν) sector. IceCube

527 demonstrated that we are sensitive to neutrinos in regions that correlate with significant photon
 528 emission like the galactic plane [22]. Neutrinos, like gravitational waves and light, travel mostly
 529 unimpeded from their source to our observatories. This makes pointing to the originating source
 530 of these messengers much easier than it is for cosmic rays which are deflected from their source by
 531 magnetic fields.

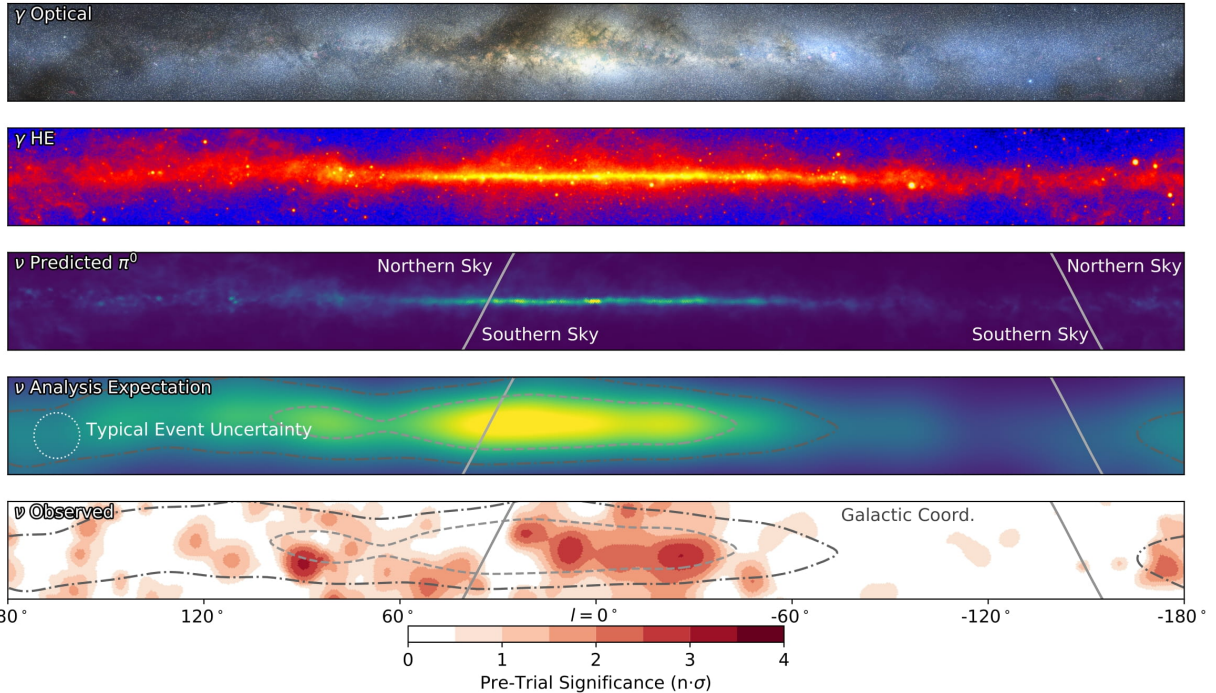


Figure 2.13 The Milky Way Galaxy in photons (γ) and neutrinos (ν) [22]. The Galactic center is at $l=0^\circ$ and is the brightest region in all panels. (top) An Optical color image of the Milky Way galaxy seen from Earth. Clouds of gas and dust obscure some light from stars. (2nd down) Integrated flux of γ -rays observed by the Fermi-LAT telescope [23]. (middle) Expected neutrino emission that corresponds with Fermi-LAT observations. (2nd up) Expected neutrino emission profile after considering detector systematics of IceCube. (bottom) Observed neutrino emission from region of the galactic plane. Substantial neutrino emission was detected.

532 The IceCube collaboration recently published a groundbreaking result of the Milky Way in
 533 neutrinos. The recent result from IceCube, shown in Figure 2.13, proves that we can make
 534 observations under different messenger regimes. The top two panels show the appearance of the
 535 galactic plane to different wavelengths of light. Some sources are more apparent in some panels,
 536 while others are not. This new channel is powerful because neutrinos are readily able to penetrate
 537 through gas and dust in the Milky Way. This new image also refines our understanding of how high

538 energy particles are produced. For example, the fit to IceCube data prefers neutrino production
 539 from the decay of π^0 [22].

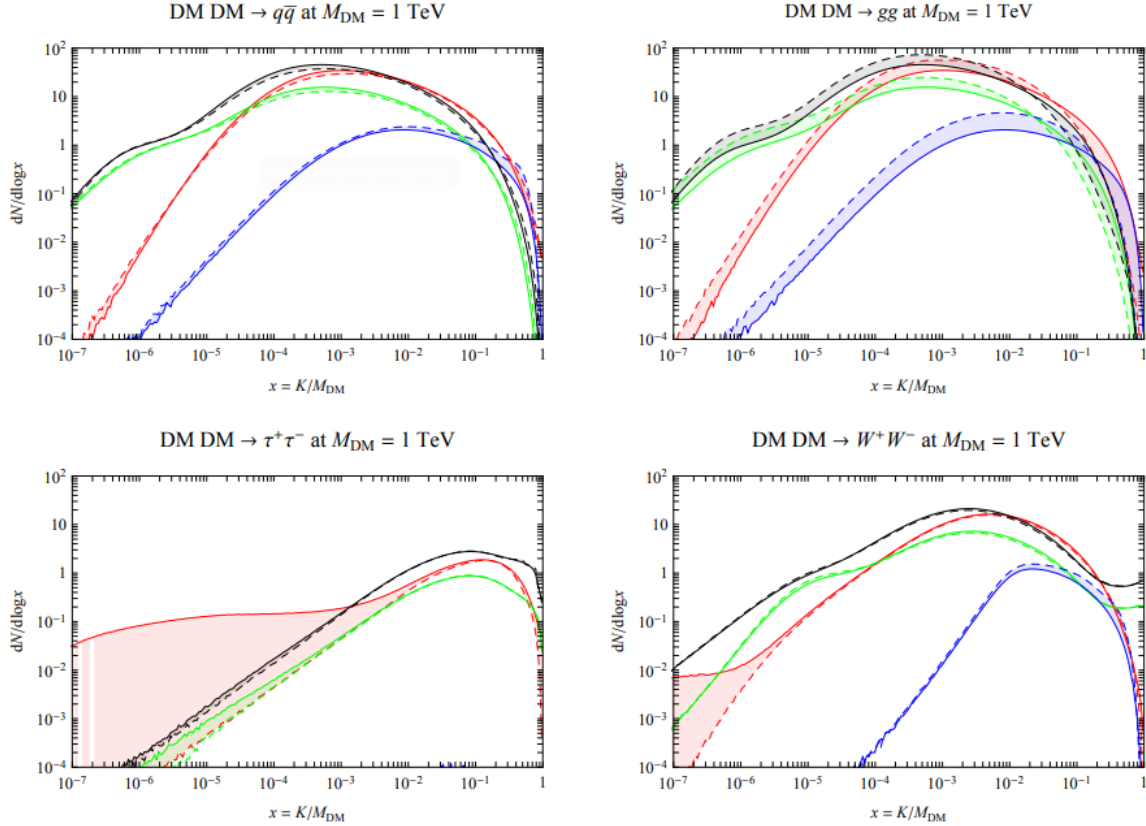


Figure 2.14 Dark Matter annihilation spectra for different final state particle and standard model annihilation channels [24]. Photons (red), e^\pm (green), \bar{p} (blue), ν (black).

540 Exposing our observations to more cosmic messengers greatly increases our sensitivity to
 541 rare processes. In the case of DM, Figure 2.14, there are many SM particles produced in DM
 542 annihilation. Among the final state fluxes are gammas and neutrinos. Charged particles are also
 543 produced however they would not likely make it to Earth since they will be deflected by magnetic
 544 fields between the source and Earth. This means observatories that can see the neutral messengers
 545 are especially good for DM searches and for combining data for a multi-messenger DM search.

CHAPTER 3

546 MULTIMESSENGER ASTROPHYSICS: DETECTING HIGH ENERGY NEUTRAL 547 MESSENGERS

548 3.1 Introduction

549 Before the 20th century, all astrophysics observations were optical in nature. We literally only
550 saw things with highly magnified optical observations. Then we discovered cosmic rays. cosmic
551 rays are charged particles, typically naked protons or H+. This was seen by Victor Hess in 19??.
552 Around the same time we discovered neutrinos from beta decay. Sometime around 1950 we started
553 to build neutrino detectors which were mostly sensitive to neutrinos from the sun. Finally, it was
554 theorized that compact objects like black holes and neutron stars would create waves in space-time
555 when they experience mergers or collisions.

556 In the 21st century, we have developed new observation techniques and detectors that are no only
557 sensitive to these four messengers - photons ([TODO: photon](#)), neutrinos ([TODO: nu](#)), Cosmic
558 Rays (CR), and Gravitational Wave (WV) - we're collect high energy versions of these events.
559 For the standad model particles, we're now sensitive to all messengers above the MeV eneryg
560 range. Additionally, the GW's were sensitive to are in the stellar mass black hole region and above
561 within our galactic neighborhood. This means were becoming sensitive to the fundamental physics
562 occuring within the universe and we can rely on the universe as a TeV+ particle accelerator. We
563 also have the abaility to correlate high energy events across messengers and gain new insights on
564 the processes that occur in our universe.

565 This thesis focuses on very high energy (VHE) gamma rays and neutrinos. These can both be
566 observed through the water cherenkov detection technique altho not exclusively. Methods on how
567 to detect and observe these neutral messengers are discussed Section 3.3 and Section 3.4

568 3.2 Charged Particles in a Medium

569 For high enery gamma-rays and neutrinos, we can exploit the same effect that charged particles
570 have with water. This effect is known as Cherenkov radiation. Cherenkov Radiation occurs when a
571 charged particle, usually electrons (e) or muons (μ), traverse a medium, like water, faster than the

572 speed of light in that medium. This is similar to sonic boom where an object moves through air
573 faster than the speed of sound in air. Cherenkov radiation can therefore be thought of as an 'optic
574 boom'. Many astro-particle physics experiments will use water as the medium as because water
575 has a unique set of properties ideal for charged particle tracking.



Figure 3.1 TODO: Show a nuclear reactor with cherenkov radiation[NEEDS A SOURCE][FACT CHECK THIS]

576 The frequency of light emitted due to cherenkov radiation follows the equation:

$$INSERT\ Cherenkov\ wavelength\ calc\ HERE. \quad (3.1)$$

577 The absorption spectra is shown in the following figure:

578 **3.3 Photons (γ)**

579 **3.4 Neutrinos (ν)**

580 **3.5 Opportunities to Combine for Dark Matter**



Figure 3.2 TODO: absorption spectrum of liquid and solid water[NEEDS A SOURCE][FACT CHECK THIS]

CHAPTER 4

581 **HIGH ALTITUDE WATER CHERENKOV (HAWC) OBSERVATORY**

582 **4.1 The Detector**

583 **4.2 Events Reconstruction and Data Acquisition**

584 **4.2.1 G/H Discrimination**

585 **4.2.2 Angle**

586 **4.2.3 Energy**

587 **4.3 Remote Monitoring**

588 **4.3.1 ATHENA Database**

589 **4.3.2 HOMER**

590

CHAPTER 5

ICECUBE NEUTRINO OBSERVATORY

591 **5.1 The Detector**

592 **5.2 Events Reconstruction and Data Acquisition**

593 **5.2.1 Angle**

594 **5.2.2 Energy**

595 **5.3 Northern Test Site**

596 **5.3.1 PIgeon remote dark rate testing**

597 **5.3.2 Bulkhead Construction**

CHAPTER 6

COMPUTATIONAL TECHNIQUES IN PARTICLE ASTROPHYSICS

599 **6.1 Neural Networks for Gamma/Hadron Separation**

600 **6.2 Parallel Computing for Dark Matter Analyses**

CHAPTER 7

GLORY DUCK: MULTI-WAVELENGTH SEARCH FOR DARK MATTTER ANNIHILATION TOWARDS DWARF SPHEROIDAL GALAXIES

7.1 Introduction

The field of astrophysics now has several instruments and observatories sensitive to high energy gamma-rays. The energy sensitivity for the modern gamma-ray program spans many orders of magnitude. Figure 7.1 demonstrates these similar sensitivities across energies for the five experiments: Fermi-LAT, HAWC, HESS, MAGIC, and VERITAS.

Each of the five experiments featured in Figure 7.1 have independently searched for DM annihilation from dwarf spheroidal galaxies (dSph) and set limits. Intriguingly, there are regions of substantial overlap in their energy sensitivities. This clearly motivates an analysis that combines data from these five. Each experiment has unique gamma-ray detection methods and their weaknesses and strengths can be leveraged with each other. The HAWC gamma-ray observatory is extensively introduced in chapter 4, so it is not introduced here. A brief description of the remaining experiments are in the following paragraphs.

The Large Area Telescope (LAT) is a pair conversion telescope mounted on the NASA Fermi satellite in orbit \sim 550 km above the Earth [25]. LAT's field of view covers about 20% of the whole sky, and it sweeps the whole sky approximately every 3 hours. LAT's gamma-ray energy sensitivity ranges from 20 MeV up to 1 TeV. Previous DM searches towards dSphs using Fermi-LAT are published in [26] and [27]

The High Energy Spectroscopic System (HESS), Major Atmospheric Gamma Imaging Cherenkov (MAGIC), and Very Energetic Radiation Imaging Telescope Array System (VERITAS) are arrays of Imaging Atmospheric Cherenkov Telescopes (IACT). These telescopes observe the Cherenkov light emitted from gamma-ray showers in the Earth's atmosphere. The field of view for these telescopes is no larger than 5° with energy sensitivities ranging from 30 GeV up to 100 TeV [28, 29, 30]. IACTs are able to make precise observations in selected regions of the sky, however can only be operated in ideal dark conditions. HESS's observations of the dwarves

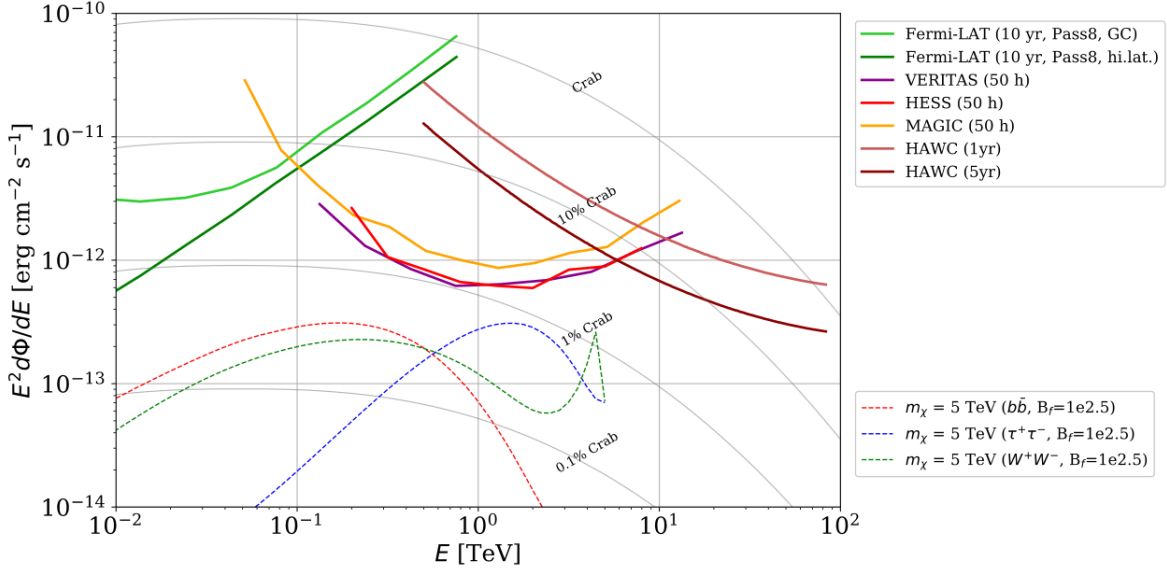


Figure 7.1 [NEEDS A SOURCE] Sensitivities of five gamma-ray experiments compared to percentages of the Crab nebula's emission and dark matter annihilation. Solid lines present estimated sensitivities to power law spectra [FACT CHECK THIS] for each experiment. Green lines are Fermi-LAT sensitivities where lighter green is the sensitivity to the galactic center and dark green is its sensitivity to higher declinations. Orange, red, and purple solid lines represent the MAGIC, HESS, and VERITAS 50 hour sensitivities respectively. The maroon and brown lines are the HAWC 1 year and 5 year sensitivities. Across four decades of gamma-ray energy, these experiments have similar sensitivities on the order 10^{-12} erg cm $^{-2}$ s $^{-1}$. The dotted lines are estimated dark matter fluxes assuming $m_\chi = 5$ TeV DM annihilating to bottom quarks (red), tau leptons (blue), and W bosons (green). Faded gray lines outline percentage flux of the Crab nebula.

627 Sculptor and Carina were between January 2008 and December 2009. HESS's observations of
 628 Coma Berenices were from 2010 to 2013, and Fornax was observed in 2010 [31, 32, 33]. MAGIC
 629 provided deep observations of Segue1 between 2011 and 2013 [34]. MAGIC also provides data
 630 for three dwarves: Coma Berenices, Draco, and Ursa Major II where observations were made
 631 in: January - June 2019 [35], March - September 2018 [35], and 2014 - 2016 [36] respectively.
 632 VERITAS provided data for Boötes I, Draco, Segue 1, and Ursa Minor from 2009 to 2016 [37].

633 This chapter presents the Glory Duck analysis, the name given for the search for dark matter
 634 annihilation from dSph by combining data from the five gamma-ray observatories: Fermi-LAT,
 635 HAWC, HESS, MAGIC, and VERITAS. Specifically, the methods in analysis and modeling are
 636 presented for the HAWC gamma-ray observatory. This work was published to the Journal of
 637 Cosmology and Astroparticle Physics and presented at the International Cosmic Ray Conference

638 in 2019, 2021, and 2023 [38, 39, 40] and others.

639 **7.2 Dataset and Background**

640 This section enumerates the data and background methods used for HAWC’s study of dSphs.
641 Section 7.2.1 and Section 7.2.2 are most useful for fellow HAWC collaborators looking to replicate
642 the Glory Duck analysis.

643 **7.2.1 Itemized HAWC files**

- 644 • Detector Resolution: `response_aerie_svn_27754_systematics_best_mc_test_no`
645 `broadpulse_10pctlogchargesmearing_0.63qe_25kHzNoise_run5481_curvatu`
646 `re0_index3.root`
- 647 • Data Map: `maps-20180119/liff/maptree_1024.root`
- 648 • Spectral Dictionary: `DM_CirrelliSpectrum_dict_gammas.npy`
- 649 • Analysis wiki: https://private.hawc-observatory.org/wiki/index.php/Glory_Duck_Multi-Experiment_Dark_Matter_Search

651 **7.2.2 Software Tools and Development**

652 This analysis was performed using HAL and 3ML [41, 42] in Python version 2. I built software
653 to implement the *A Poor Particle Physicist Cookbook for Dark Matter Indirect Detection* (PPPC)
654 [43] DM spectral model and dSphs spatial model from [44] for HAWC analysis. A NumPy version
655 of this dictionary was made for both Py2 and Py3. The code base for creating this dictionary is
656 linked on my GitLab sandbox:

- 657 • Py2: [Dictionary Generator \(Deprecated\)](#)
- 658 • Py3: [PPPC2Dict](#)

659 The analysis was performed using the f_{hit} framework performed in the HAWC Crab paper
660 [41]. The Python2 NumPy dictionary file for gamma-ray final states is `dmCirSpecDict.npy`. The
661 corresponding Python3 file is `DM_CirrelliSpectrum_dict_gammas.npy`. These files can also

662 be used for decay channels and the PPPC describes how [43]. All other software used for data
663 analysis, DM profile generation, and job submission to SLURM are also kept in my sandbox for
664 [the Glory Duck](#) project.

665 **7.2.3 Data Set and Background Description**

666 The HAWC data maps used for this analysis contain 1017 days of data between runs 2104
667 (2014-11-26) and 7476 (2017-12-20). They were generated from pass 4.0 reconstruction. The
668 analysis is performed using the f_{hit} energy binning scheme with bins (1-9) similar to what was done
669 for the Crab and previous HAWC dSph analysis [41, 45]. Bin 0 was excluded as it has substantial
670 hadronic contamination and poor angular resolution.

671 This analysis was done on dSphs because of their large DM mass content relative to baryonic
672 mass. We consider the following to estimate the background to this study.

- 673 • The dSphs are small in HAWC’s field of view, so the analysis is not sensitive to large or small
674 scale anisotropies.
- 675 • The dSphs used in this analysis are off the galactic plane.
- 676 • The dSphs are baryonically faint relative to their expected dark matter content and are not
677 expected to contain high energy gamma-ray sources.

678 Therefor we make no additional assumptions on the background from our sources and use
679 HAWC’s standard direct integration method for background estimation [41]. It is possible for
680 gamma rays from DM annihilation to scatter in transit to HAWC via Inverse Compton Scattering
681 (ICS). This was investigated and its impact on the flux is basically zero. Supporting information
682 on this is in Section 7.6.1

683 **7.3 Analysis**

684 The expected differential photon flux from DM-DM annihilation to standard model particles,
685 $d\Phi_\gamma/dE_\gamma$, over solid angle, Ω is described by the familiar equation.

$$\frac{d\Phi_\gamma}{dE_\gamma} = \frac{\langle\sigma v\rangle}{8\pi m_\chi^2} \frac{dN_\gamma}{dE_\gamma} \times \int_{\text{source}} d\Omega \int_{l.o.s} \rho_\chi^2 dl(r, \theta') \quad (7.1)$$

686 Where $\langle \sigma v \rangle$ is the velocity weighted annihilation cross-section. $\frac{dN}{dE}$ is the expected differential
 687 number of photons produced at each energy per annihilation. m_χ is the rest mass of the supposed
 688 DM particle. ρ_χ is the DM density. J is the astrophysical J-factor and is defined as

$$J = \int d\Omega \int_{l.o.s} dl \rho_\chi^2(r, \theta') \quad (7.2)$$

689 l is the distance to the source from Earth. r is the radial distance from the center of the source. θ' is
 690 the half angle defining a cone containing the DM source. How each component is synthesized and
 691 considered for HAWC's analysis is presented in the following sections. Section 7.3.1 presents the
 692 particle physics model for DM annihilation. Section 7.3.2 presents the spatial distributions built
 693 for each dSph.

694 7.3.1 $\frac{dN_\gamma}{dE_\gamma}$ - Particle Physics Component

695 For these spectra, we import the PPPC with Electroweak (EW) corrections [43]. The spectrum
 696 is implemented as a model script in astromodels for 3ML. The EW corrections were previously not
 697 considered for HAWC and are significant for DM annihilating to EW coupled SM particles such
 698 as all leptons, and the γ , Z , and W bosons [45]. Figure 7.2 demonstrates the significance of EW
 699 corrections for W boson annihilation. Across EW SM channels, the gamma-ray spectra become
 700 harder than spectra without EW corrections. Tables from the PPPC were reformatted into Python
 701 NumPy dictionaries for collaboration-wide use. A class in astromodels was developed to include
 702 the EW correction from the PPPC and is aptly named `PPPCSpectra` within `DM_models.py`.

703 7.3.2 J - Astrophysical Component

704 The J-factor profiles for each source are imported from Geringer-Sameth (referred to with \mathcal{GS})
 705 [44]. These were pulled from the publication as $J(\theta)$, where θ is the angular separation from the
 706 center of the source. HAWC requires maps in terms of $\frac{dJ}{d\Omega}$, so the conversion from the maps was
 707 done in the following way...

708 First, convert the angular distances to solid angles

$$\Omega = 2 \cdot \pi(1 - \cos(\theta)) \quad (7.3)$$

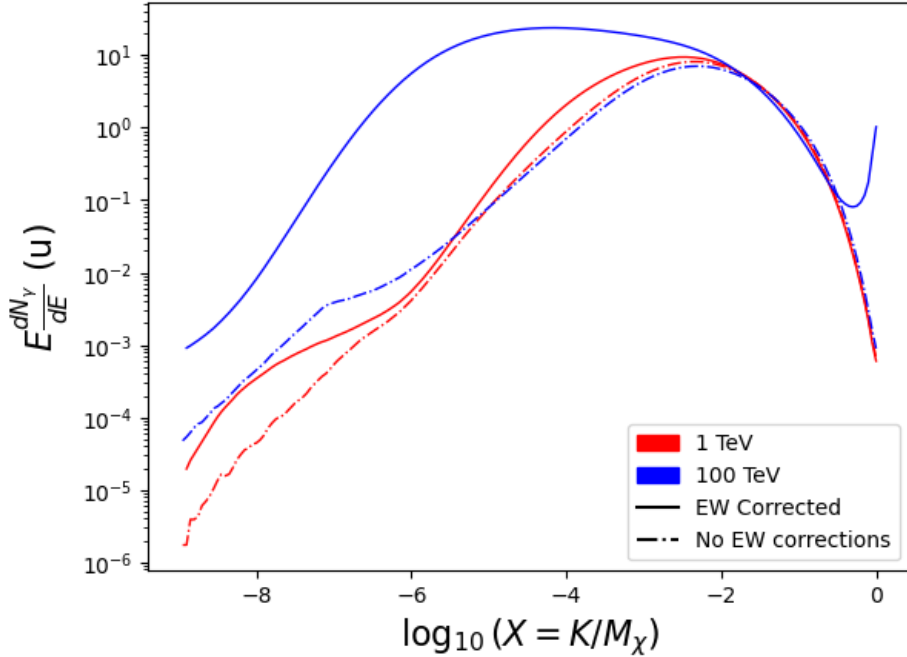


Figure 7.2 Effect of Electro-Weak (EW) corrections on expected DM annihilation spectrum for $\chi\chi \rightarrow W^-W^+$. Solid lines are spectral models that consider EW corrections. Dash-dot lines are spectral models without EW corrections. Red lines are models for $M_\chi = 1$ TeV. Blue lines represent models for $M_\chi = 100$ TeV. All models are sourced from the PPPC4DMID [43].

709 which reduces with a small angle approximation to $\pi\theta^2$. Next, the central difference for both the
 710 ΔJ and $\Delta\Omega$ value were calculated from the discretized $J(\theta)$ with the central difference stencil:

$$\Delta\phi_i = \phi_{i+1} - \phi_{i-1} \quad (7.4)$$

711 Where ϕ is either Ω or J . These were done separately in case the grid spacing in θ was not uniform.
 712 Finally, these lists are divided so that we are left with an approximation of the $dJ/d\Omega$ profile that
 713 is a function of θ . Admittedly, this is an approximation method for the map which introduces small
 714 errors compared to the true profile estimate. This was checked as a systematic against the author's
 715 profiling of the spatial distribution and is documented in Section 7.7.1.

716 With $\frac{dJ}{d\Omega}(\theta)$, a map is generated, first by filling in the north-east quadrant of the map. This
 717 quadrant is then reflected twice, vertically then horizontally, to fill the full map. Maps are then
 718 normalized by dividing the discrete 2D integral of the map. The 2D integral was a simple height

719 of bins, Newton’s integral:

$$p^2 \cdot \sum_{i,j=0}^{N,M} \frac{dJ}{d\Omega}(\theta_{i,j}) \quad (7.5)$$

720 These maps are HEALpix maps with NSIDE 16384 and saved in the `.fits` format.

721 Another DM spatial distribution model from Bonnivard (\mathcal{B}) [46] was used for the Glory Duck
722 study. However, to save computational time, limits from \mathcal{GS} were scaled to \mathcal{B} instead of each
723 experiment performing a full study a second time. How these models compare is demonstrated
724 for each dSph in Figure 7.15 and Figure 7.16 Plots of these maps are provided for each source
725 in chapter A Examples of the two most impactful dSphs derived from \mathcal{GS} , Segue1 and Coma
726 Berenices are featured in Figure 7.3

727 7.3.3 Source Selection and Annihilation Channels

728 We use many of the dSphs presented in HAWC’s previous dSph DM search [45]. HAWC’s
729 sources for Glory Duck include Boötes I, Coma Berenices, Canes Venatici I + II, Draco, Hercules,
730 Leo I, II, + IV, Segue 1, Sextans, and Ursa Major I + II. A full description of all sources used
731 in Glory Duck is found in Table 7.1. Triangulum II was excluded from the Glory Duck analysis
732 because of large uncertainties in its J factor. Ursa Minor was excluded from HAWC’s contribution
733 to the combination because the source extension model extended Ursa Minor beyond HAWC’s field
734 of view. Ursa Minor was not expected to contribute significantly to the combined limit, so work
735 was not invested in a solution to include Ursa Minor.

736 This analysis improves on the previous HAWC dSph paper [45] in the following ways. Pre-
737 viously, the dSphs were treated and implemented as point sources. For this analysis, dSphs are
738 modeled and treated as extended source. The impact of this change with respect to the upper limit
739 is source dependant and is explored in Section 7.6.2 Previously, the particle physics model used for
740 gamma-ray spectra from DM annihilation did not have EW corrections where the PPPC includes
741 them. Finally, the gamma-ray dataset is much larger. The study performed here analyzes over
742 1000 days of data compared to 507.

743 The SM annihilation channels probed for the Glory Duck combination include $b\bar{b}$, $e\bar{e}$, $\mu\bar{\mu}$, $\tau\bar{\tau}$,
744 $t\bar{t}$, W^+W^- , and ZZ . A summary of all sources, with a description of each experiments’ sensitivity

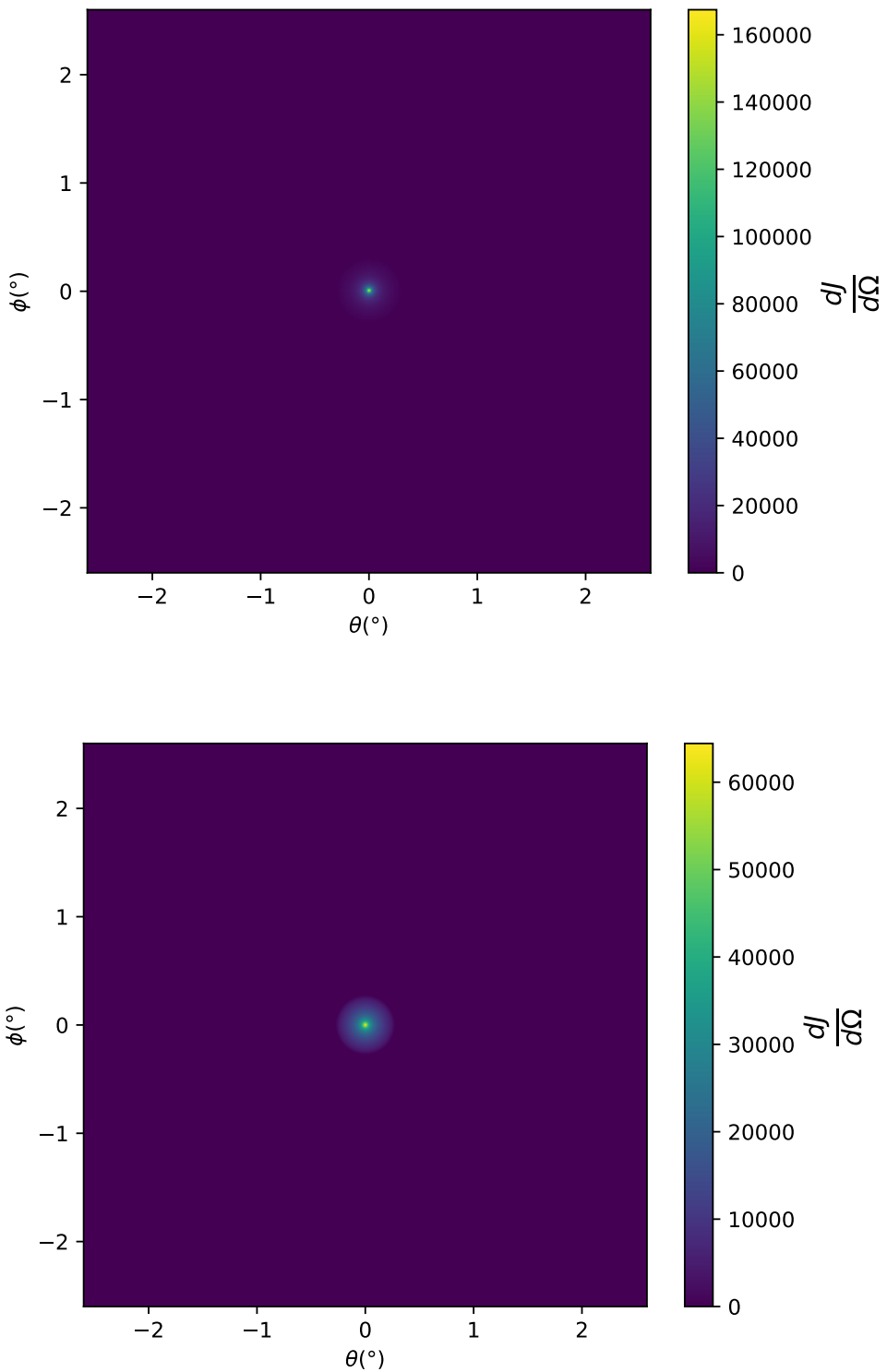


Figure 7.3 $\frac{dJ}{d\Omega}$ maps for Segue1 (top) and Coma Berenices (bottom). Origin is centered on the specific dwarf spheroidal galaxies (dSph). X and Y axes are the angular separation from the center of the dwarf. Plots of the remaining 11 dSph HAWC studied are linked in Fig. A.1.

745 to the source, is provided in Table 7.2.

Table 7.1 Summary of the relevant properties of the dSphs used in the present work. Column 1 lists the dSphs. Columns 2 and 3 present their heliocentric distance and galactic coordinates, respectively. Columns 4 and 5 report the J -factors of each source given from the \mathcal{GS} and \mathcal{B} independent studies and their estimated $\pm 1\sigma$ uncertainties. The values $\log_{10} J$ (\mathcal{GS} set) [44] correspond to the mean J -factor values for a source extension truncated at the outermost observed star. The values $\log_{10} J$ (\mathcal{B} set) [46] are provided for a source extension at the tidal radius of each dSph. **Bolded sources are within HAWC's field of view and provided to the Glory Duck analysis.**

Name	Distance (kpc)	l, b ($^{\circ}$)	$\log_{10} J$ (\mathcal{GS} set) $\log_{10}(\text{GeV}^2\text{cm}^{-5}\text{sr})$	$\log_{10} J$ (\mathcal{B} set) $\log_{10}(\text{GeV}^2\text{cm}^{-5}\text{sr})$
Boötes I	66	358.08, 69.62	$18.24^{+0.40}_{-0.37}$	$18.85^{+1.10}_{-0.61}$
Canes Venatici I	218	74.31, 79.82	$17.44^{+0.37}_{-0.28}$	$17.63^{+0.50}_{-0.20}$
Canes Venatici II	160	113.58, 82.70	$17.65^{+0.45}_{-0.43}$	$18.67^{+1.54}_{-0.97}$
Carina	105	260.11, -22.22	$17.92^{+0.19}_{-0.11}$	$18.02^{+0.36}_{-0.15}$
Coma Berenices	44	241.89, 83.61	$19.02^{+0.37}_{-0.41}$	$20.13^{+1.56}_{-1.08}$
Draco	76	86.37, 34.72	$19.05^{+0.22}_{-0.21}$	$19.42^{+0.92}_{-0.47}$
Fornax	147	237.10, -65.65	$17.84^{+0.11}_{-0.06}$	$17.85^{+0.11}_{-0.08}$
Hercules	132	28.73, 36.87	$16.86^{+0.74}_{-0.68}$	$17.70^{+1.08}_{-0.73}$
Leo I	254	225.99, 49.11	$17.84^{+0.20}_{-0.16}$	$17.93^{+0.65}_{-0.25}$
Leo II	233	220.17, 67.23	$17.97^{+0.20}_{-0.18}$	$18.11^{+0.71}_{-0.25}$
Leo IV	154	265.44, 56.51	$16.32^{+1.06}_{-1.70}$	$16.36^{+1.44}_{-1.65}$
Leo V	178	261.86, 58.54	$16.37^{+0.94}_{-0.87}$	$16.30^{+1.33}_{-1.16}$
Leo T	417	214.85, 43.66	$17.11^{+0.44}_{-0.39}$	$17.67^{+1.01}_{-0.56}$
Sculptor	86	287.53, -83.16	$18.57^{+0.07}_{-0.05}$	$18.63^{+0.14}_{-0.08}$
Segue I	23	220.48, 50.43	$19.36^{+0.32}_{-0.35}$	$17.52^{+2.54}_{-2.65}$
Segue II	35	149.43, -38.14	$16.21^{+1.06}_{-0.98}$	$19.50^{+1.82}_{-1.48}$
Sextans	86	243.50, 42.27	$17.92^{+0.35}_{-0.29}$	$18.04^{+0.50}_{-0.28}$
Ursa Major I	97	159.43, 54.41	$17.87^{+0.56}_{-0.33}$	$18.84^{+0.97}_{-0.43}$
Ursa Major II	32	152.46, 37.44	$19.42^{+0.44}_{-0.42}$	$20.60^{+1.46}_{-0.95}$
Ursa Minor	76	104.97, 44.80	$18.95^{+0.26}_{-0.18}$	$19.08^{+0.21}_{-0.13}$

746 7.3.4 Likelihood Methods

747 We perform a standard HAWC binned maximum likelihood analysis using f_{hit} bins 1-9. we
 748 compute the max from the likelihood profiles and perform a ratio test to calculate the significance

Table 7.2 Summary of dSph observations by each experiment used in this work. A ‘-’ indicates the experiment did not observe the dSph for this study. For Fermi-LAT, the exposure at 1 GeV is given. For HAWC, $|\Delta\theta|$ is the absolute difference between the source declination and HAWC latitude. HAWC is more sensitive to sources with smaller $|\Delta\theta|$. For IACTs, we show the zenith angle range, the total exposure, the energy range, the angular radius θ of the signal or ON region, the ratio of exposures between the background-control (OFF) and signal (ON) regions (τ), and the significance of gamma-ray excess in standard deviations, σ .

Source name	Fermi-LAT	HAWC	H.E.S.S, MAGIC, VERITAS						
	Exposure (10^{11} s m 2)	$ \Delta\theta $ ($^\circ$)	IACT	Zenith ($^\circ$)	Exposure (h)	Energy range (GeV)	θ ($^\circ$)	τ	S (σ)
Boötes I	2.6	4.5	VERITAS	15 – 30	14.0	100–41000	0.10	8.6	-1.0
Canes Venatici I	2.9	14.6	–	–	–	–	–	–	–
Canes Venatici II	2.9	15.3	–	–	–	–	–	–	–
Carina	3.1	–	H.E.S.S.	27 – 46	23.7	310 – 70000	0.10	18.0	-0.3
Coma Berenices	2.7	4.9	H.E.S.S.	47 – 49	11.4	550 – 70000	0.10	14.4	-0.4
Draco	3.8	38.1	MAGIC	5 – 37	49.5	60 – 10000	0.17	1.0	–
			MAGIC	29 – 45	52.1	70 – 10000	0.22	1.0	–
			VERITAS	25 – 40	49.8	120 – 70000	0.10	9.0	-1.0
Fornax	2.7	–	H.E.S.S.	11 – 25	6.8	230 – 70000	0.10	45.5	-1.5
Hercules	2.8	6.3	–	–	–	–	–	–	–
Leo I	2.5	6.7	–	–	–	–	–	–	–
Leo II	2.6	3.1	–	–	–	–	–	–	–
Leo IV	2.4	19.5	–	–	–	–	–	–	–
Leo V	2.4	–	–	–	–	–	–	–	–
Leo T	2.6	–	–	–	–	–	–	–	–
Sculptor	2.7	–	H.E.S.S.	10 – 46	11.8	200 – 70000	0.10	19.8	-2.2
Segue I	2.5	2.9	MAGIC	13 – 37	158.0	60 – 10000	0.12	1.0	-0.5
			VERITAS	15 – 35	92.0	80 – 50000	0.10	7.6	0.7
Segue II	2.7	–	–	–	–	–	–	–	–
Sextans	2.4	20.6	–	–	–	–	–	–	–
Ursa Major I	3.4	32.9	–	–	–	–	–	–	–
Ursa Major II	4.0	44.1	MAGIC	35 – 45	94.8	120 – 10000	0.30	1.0	-2.1
Ursa Minor	4.1	–	VERITAS	35 – 45	60.4	160 – 93000	0.10	8.4	-0.1

749 of each source. This analysis is identical to the previous dSph analysis [45] except the sources are
 750 treated as extended. For the vast majority of our sources, this extension is no greater than 2 degrees.
 751 We calculate the likelihood of each source and model, assuming events are Poisson distributed,
 752 with

$$\mathcal{L} = \prod_i \frac{(B_i + S_i)^{N_i} e^{-(B_i + S_i)}}{N_i!} \quad (7.6)$$

754 S_i is the sum of expected number of signal counts. B_i is the number of background counts
 755 observed. N_i is the total number of counts. The i th bin is iterated over spatial and f_{hit} . Then we
 756 combine the profiles across all five experiments. The profile likelihood ratio λ as a function of
 757 annihilation cross-section $\langle\sigma v\rangle$ is computed by:

$$\lambda(\langle\sigma v\rangle | \mathcal{D}_{\text{dSphs}}) = \frac{\mathcal{L}(\langle\sigma v\rangle; \hat{\nu} | \mathcal{D}_{\text{dSphs}})}{\mathcal{L}(\widehat{\langle\sigma v\rangle}; \hat{\nu} | \mathcal{D}_{\text{dSphs}})} \quad (7.7)$$

758 for a considered annihilation channel and DM mass.

759 **TODO: Section pasted from paper. Rephrase cause plagiarism is a thing.** As mentioned pre-
 760 viously, each experiment computes the \mathcal{L}_{lk} from Equation (7.7) differently. The remainder of
 761 this section highlights the differences in this calculation across the experiments. Four experiments,
 762 namely *Fermi*-LAT, H.E.S.S., HAWC and MAGIC, use a binned likelihood to compute the \mathcal{L}_{lk} . For
 763 these experiments, for each observation \mathcal{D}_{lk} of a given dSph l carried out using a given gamma-ray
 764 detector k , the binned likelihood function is:

$$\mathcal{L}_{lk}(\langle\sigma v\rangle; J_l, \nu_{lk} | \mathcal{D}_{lk}) = \prod_{i=1}^{N_E} \prod_{j=1}^{N_P} \left[\mathcal{P}(s_{lk,ij}(\langle\sigma v\rangle, J_l, \nu_{lk}) + b_{lk,ij}(\nu_{lk}) | N_{lk,ij}) \right] \times \mathcal{L}_{lk,\nu}(\nu_{lk} | \mathcal{D}_{\nu_{lk}}) \quad (7.8)$$

765 where N_E and N_P are the number of considered bins in reconstructed energy and arrival
 766 direction, respectively; \mathcal{P} represents a Poisson PDF for the number of gamma-ray candidate events
 767 $N_{lk,ij}$ observed in the i -th bin in energy and j -th bin in arrival direction, when the expected number
 768 is the sum of the expected mean number of signal events s_{ij} (produced by DM annihilation) and of
 769 background events b_{ij} ; $\mathcal{L}_{lk,\nu}$ is the likelihood term for the extra ν_{lk} nuisance parameters that vary
 770 from one instrument k to another. The expected counts for signal events s_{ij} for a given dSph l and
 771 detector k is given by:

$$s_{ij}(\langle\sigma v\rangle, J) = \int_{E'_{\min,i}}^{E'_{\max,i}} dE' \int_{P'_{\min,j}}^{P'_{\max,j}} d\Omega' \int_0^\infty dE \int_{\Delta\Omega_{tot}} d\Omega \int_0^{T_{\text{obs}}} dt \frac{d^2\Phi(\langle\sigma v\rangle, J)}{dEd\Omega} \text{IRF}(E', P' | E, P, t) \quad (7.9)$$

772 where E' and E are the reconstructed and true energies, P' and P the reconstructed and true
 773 arrival directions; $E'_{\min,i}$, $P'_{\min,j}$, $E'_{\max,i}$, and $P'_{\max,j}$ are their lower and upper limits of the i -th
 774 energy bin and the j -th arrival direction bin; T_{obs} is the (dead-time corrected) total observation
 775 time; t is the time along the observations; $d^2\Phi/dEd\Omega$ is the DM flux in the source region (see
 776 Equation (7.1)); and $\text{IRF}(E', P' | E, P, t)$ is the IRF, which can be factorized as the product of the
 777 effective collection area of the detector $A_{\text{eff}}(E, P, t)$, the PDFs for the energy estimator $f_E(E' | E, t)$,
 778 and arrival direction $f_P(P' | E, P, t)$ estimators. Note that for Fermi-LAT, HAWC, MAGIC, and
 779 VERITAS the effect of the finite angular resolution is taken into account through the convolution
 780 of $d\Phi/dEd\Omega$ with f_P in Equation (7.9), whereas in the cases of H.E.S.S. f_P is approximated by a
 781 delta function. This approximation has been made in order to maintain compatibility of the result
 782 with what has been previously published. The difference introduced by this approximation is $< 5\%$
 783 for all considered dSphs. **TODO: End of paper section**

784 From Equation (7.7), we can compute the test statistic (TS) with the ratio test:

$$\text{TS} = -2 \ln \left(\frac{\mathcal{L}}{\mathcal{L}^{\text{max}}} \right). \quad (7.10)$$

785 \mathcal{L}^{max} here is equivalent to $\mathcal{L}(N_i, B_i, S_i = 0)$ or no signal counts.

786 7.4 HAWC Results

787 13 of the 20 dSphs considered for the Glory Duck analysis are within HAWC's field of view.
 788 These dSph are analyzed for emission from DM annihilation according to the likelihood method
 789 described in Section 7.3.4. The 13 likelihood profiles are then combined to create a combined limit
 790 on the dark matter cross-section. This combination is done for the 7 annihilation channels used in
 791 the Glory Duck analysis. Figure 7.5 shows the combined limit for all annihilation channels with
 792 HAWC only observations. We also perform 300 studies of Poisson trials on the background. These
 793 trials are used to produce HAWC Brazil bands which were shared with the other collaborators for

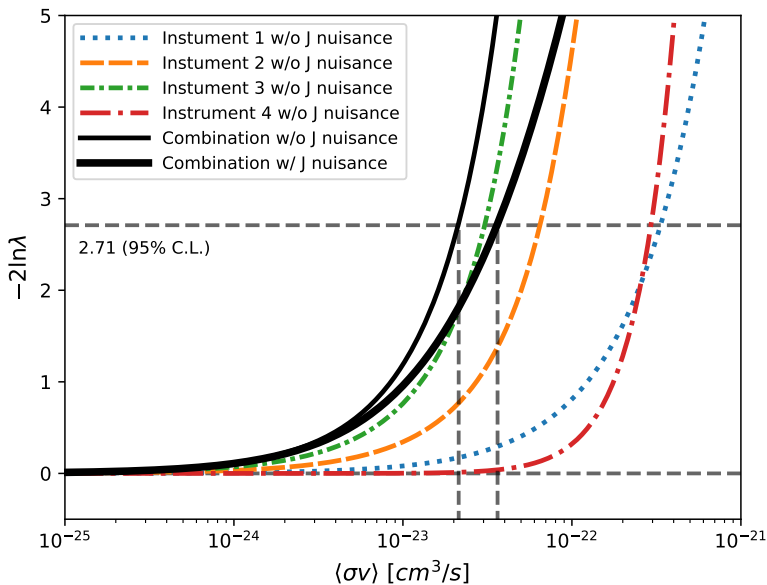


Figure 7.4 Illustration of the combination technique showing a comparison between $-2 \ln \lambda$ provided by four instruments (colored lines) from the observation of the same dSph without any J nuisance and their sum, *i.e.* the resulting combined likelihood (thin black line). According to the test statistics of Equation (7.10), the intersection of the likelihood profiles with the line $-2 \ln \lambda = 2.71$ indicates the 95% C.L. upper limit on $\langle \sigma v \rangle$. The combined likelihood (thin black line) shows a smaller value of upper limit on $\langle \sigma v \rangle$ than those derived by individual instruments. We also show the uncertainties on the J -factor affects the combined likelihood and degrade the upper limit on $\langle \sigma v \rangle$ (thick black line). All likelihood profiles are normalized so that the global minimum $\widehat{\langle \sigma v \rangle}$ is 0. We note that each profile depends on the observational conditions in which a target object was observed. The sensitivity of a given instrument can be degraded and the upper limits less constraining if the observations are performed in non optimal conditions such as a high zenith angle or a short exposure time.

794 combined Brazil Bands. The results on fitting to HAWC's poisson trials of the DM hypothesis is
 795 shown in Figure 7.6 for seven of the DM annihilation channels.

796 No DM was found in HAWC observations. The limits are dominated by the dSph Segue1 and
 797 Coma Berenices. The remaining 11 dSphs do no contribute significantly to the limit. Even though
 798 some of the remaining dSphs have large J -factors, they are towards the edge of HAWC's field of
 799 view where this analysis is less sensitive.

800 7.5 Glory Duck Combined Results

801 The crux of this analysis is that HAWC's results are combined with 4 other gamma-ray obser-
 802 vatories: Fermi-LAT, H.E.S.S., MAGIC, and VERITAS. The complete joint likelihood for the l -th

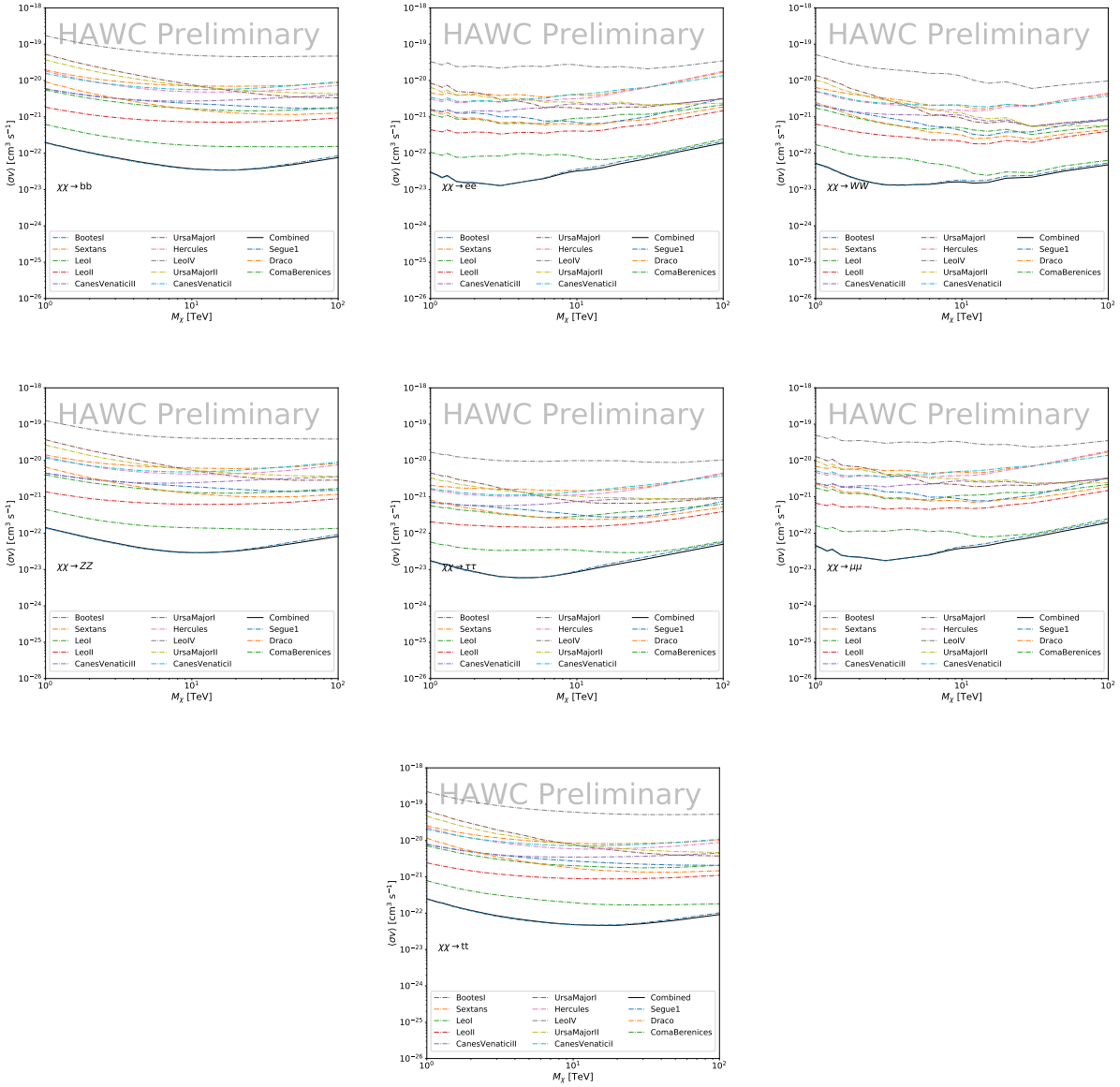


Figure 7.5 HAWC upper limits at 95% confidence level on $\langle\sigma v\rangle$ versus DM mass for seven annihilation channels, using the set of J -factors from Ref. [47]. The solid line represents the observed combined limit. Dashed lines represent limits from individual dSphs.

803 dSph is the product of likelihood functions of the 5 experiments.

804 TODO: place holder for results

805 The *partial* joint likelihood function for gamma-ray observations of each dSph ($\mathcal{L}_{dSph,I}$) is
806 written as the product of the likelihood terms describing the $N_{exp,I}$ observations performed with

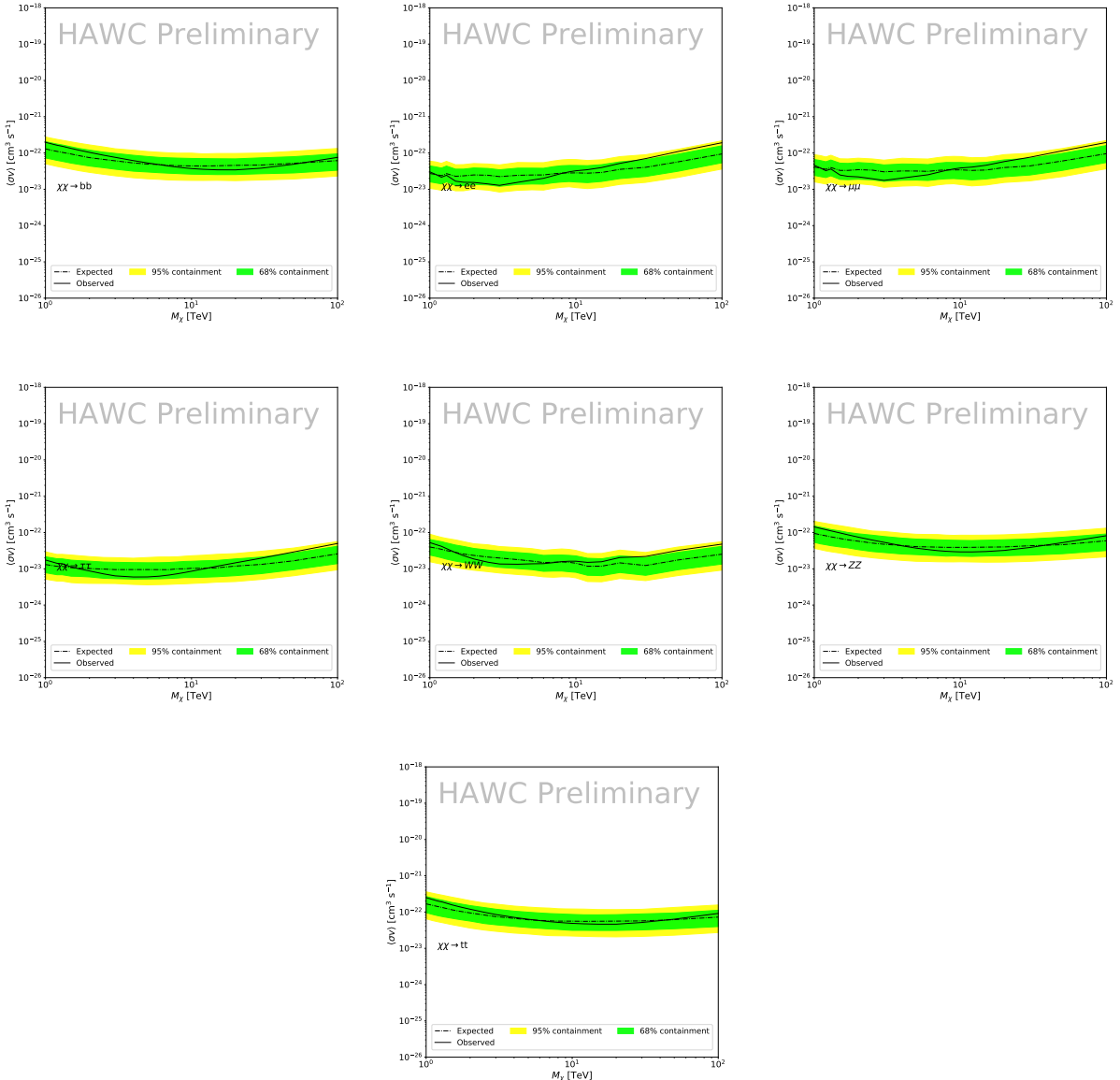


Figure 7.6 HAWC Brazil bands at 95% confidence level on $\langle\sigma v\rangle$ versus DM mass for seven annihilation channels with J -factors from \mathcal{GS} [47]. The solid line represents the combined limit from 13 dSphs. The dashed line is the expected limit. The green band is the 68% containment. The yellow band is the 95% containment.

807 any of our observatories:

$$\mathcal{L}_{\text{dSph},l} (\langle\sigma v\rangle; J_l, \nu_l | \mathcal{D}_l) = \prod_{k=1}^{N_{\text{exp},l}} \mathcal{L}_{lk} (\langle\sigma v\rangle; J_l, \nu_{lk} | \mathcal{D}_{lk}), \quad (7.11)$$

808 where each \mathcal{L}_{lk} term refers to an observation of the l -th dSph with associated k -th instrument
809 responses. $N_{\text{exp},l}$ varies from dSph to dSph and can be retrieved from Tab. 7.2.

810 Each collaboration separately analyses their data for \mathcal{D}_{lk} corresponding to dSph l and gamma-
 811 ray detector k , using as many common assumptions as possible in the analysis (see the next
 812 paragraph and further down in this section for additional details). No significant DM emission was
 813 observed by any of the five telescopes. We present upper limits on $\langle\sigma v\rangle$ using the test statistics,
 814 Eq. (7.10).

$$TS = -2 \ln \lambda(\langle\sigma v\rangle), \quad (7.12)$$

815 No significant DM emission was observed by any of the five instruments. We present the upper
 816 limits on $\langle\sigma v\rangle$ assuming seven independent DM self annihilation channels, namely W^+W^- , Z^+Z^- ,
 817 $b\bar{b}$, $t\bar{t}$, e^+e^- , $\mu^+\mu^-$, and $\tau^+\tau^-$. The 68% and 95% containment bands are produced from 300
 818 Poisson realizations of the null hypothesis corresponding to each of the combined datasets. These
 819 300 realizations are combined identically to dSph observations. The containment bands and the
 820 median are extracted from the distribution of resulting limits on the null hypothesis. These 300
 821 realizations are obtained either by fast simulations of the OFF observations, for H.E.S.S., MAGIC,
 822 VERITAS, and HAWC, or taken from real observations of empty fields of view in the case of
 823 Fermi-LAT [48, 49, 50].

824 The obtained limits are shown in Figure 7.7 for the $\mathcal{G}\mathcal{S}$ set of J -factors [47] and in Figure 7.8
 825 for the \mathcal{B} set of J -factors [46, 51]. The combined limits are presented with their 68% and 95%
 826 containment bands, and are expected to be close to the median limit when no signal is present.
 827 We observe agreement with the null hypothesis for all channels, within 2σ standard deviations,
 828 between the observed limits and the expectations given by the median limits. Limits obtained from
 829 each detector are also indicated in the figures, where limits for all dSphs observed by the specific
 830 instrument have been combined.

831 Below ~ 300 GeV, the *Fermi*-LAT dominates the DM limits for all annihilation channels. From
 832 ~ 300 GeV to ~ 2 TeV, *Fermi*-LAT continues to dominate for the hadronic and bosonic DM channels,
 833 yet the IACTs (H.E.S.S., MAGIC, and VERITAS) and *Fermi*-LAT all contribute to the limit for
 834 leptonic DM channels. For DM masses between ~ 2 TeV to ~ 10 TeV, the IACTs dominate leptonic

835 DM annihilation channels, whereas both the *Fermi*-LAT and the IACTs dominate bosonic and
836 hadronic DM annihilation channels. From ~ 10 TeV to ~ 100 TeV, both the IACTs and HAWC
837 contribute significantly to the leptonic DM limit. For hadronic and bosonic DM, the IACTs and
838 *Fermi*-LAT both contribute strongly.

839 We notice that the limits computed using the \mathcal{B} set of J -factor are always better compared to the
840 ones calculated with the \mathcal{GS} set. For the W^+W^- , Z^+Z^- , $b\bar{b}$, and $t\bar{t}$ channels, the ratio between the
841 limits computed with the two sets of J -factor is varying between a factor of ~ 3 and ~ 5 depending
842 on the energy, with the largest ratio around 10 TeV. For the channels e^+e^- , $\mu^+\mu^-$, and $\tau^+\tau^-$, the
843 ratio lies between ~ 2 to ~ 6 , being maximum around 1 TeV. Examining Figure 7.15 and Figure 7.16
844 in Section 7.7, these differences are explained by the fact that the \mathcal{B} set provides higher J -factors
845 for the majority of the studied dSphs, with the notable exception of Segue I. The variation on the
846 ratio of the limits for the two sets is due to different dSph dominating the limits depending on the
847 energy. This pushes the range of thermal cross-section which can be excluded to higher mass. This
848 comparison demonstrates the magnitude of systematic uncertainties associated with the choice of
849 the J -factor

850 This comparison demonstrates the magnitude of systematic uncertainties associated with the
851 choice of the J -factor calculation. The \mathcal{GS} and \mathcal{B} sets present a difference in the limits for all
852 channels of about This difference is explained, see Figure 7.15 and Figure 7.16 in Appendix, by the
853 fact that the \mathcal{B} set provides higher J factors for all dSph except for Segue I. This pushes the range
854 of thermal cross-section which can be excluded to higher mass.

855 7.6 HAWC Systematics

856 7.6.1 Inverse Compton Scattering

857 The DM-DM annihilation channels produce many high energy electrons regardless of the
858 primary annihilation channel. These high energy electrons can produce high energy gamma-rays
859 through Inverse Compton Scattering (ICS). If this effect is strong, it would change the morphology
860 of the source and increase the total expected gamma-ray counts from any source. The PPPC [43]
861 provides tools in Mathematica for calculating the impact of ICS for an arbitrary location in the

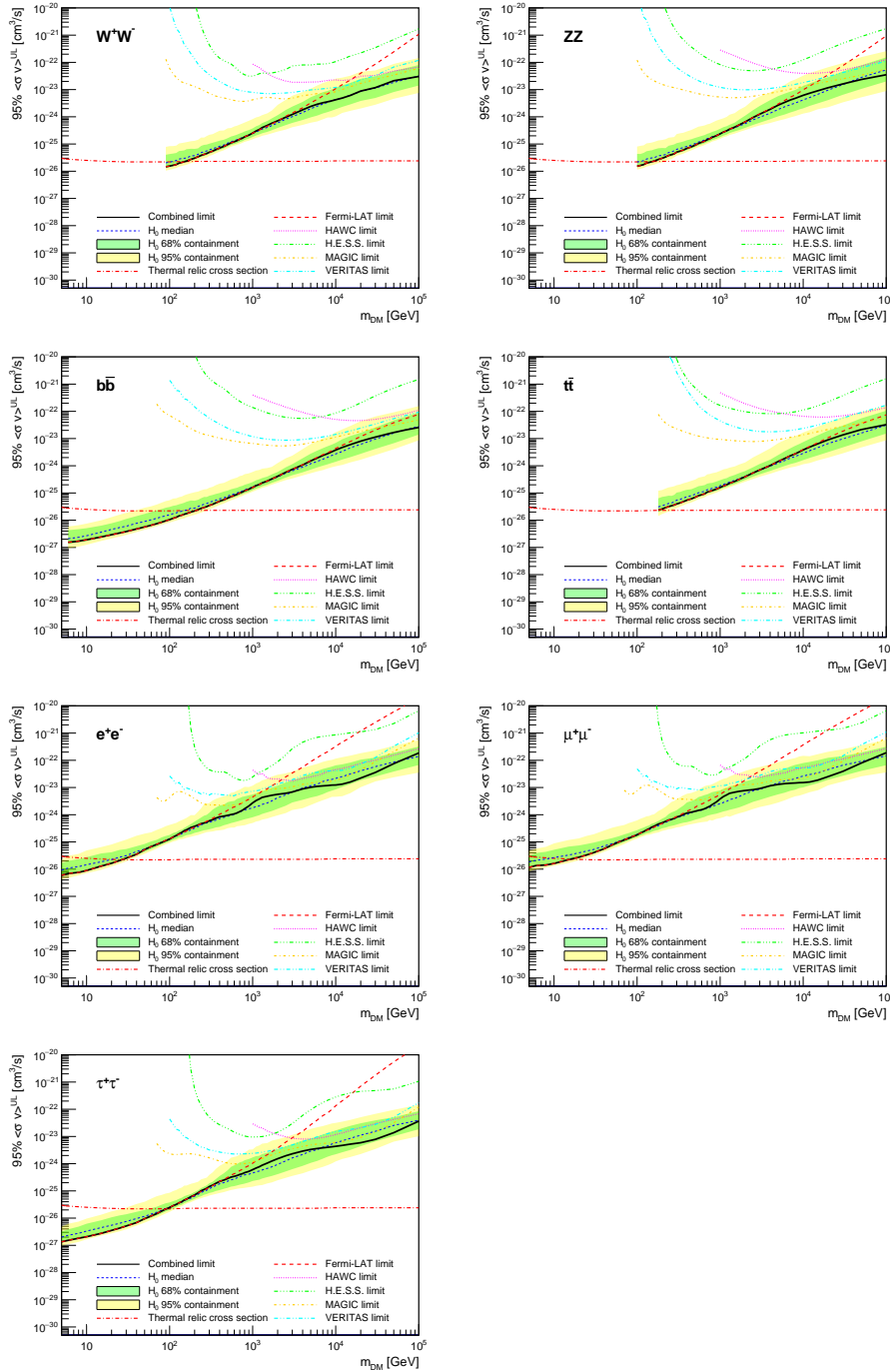


Figure 7.7 Upper limits at 95% confidence level on $\langle\sigma v\rangle$ in function of the DM mass for eight annihilation channels, using the set of J factors from Ref. [47] (\mathcal{GS} set in Table 7.1). The black solid line represents the observed combined limit, the black dashed line is the median of the null hypothesis corresponding to the expected limit, while the green and yellow bands show the 68% and 95% containment bands. Combined upper limits for each individual detector are also indicated as solid, colored lines. The value of the thermal relic cross-section in function of the DM mass is given as the red dotted-dashed line [52].

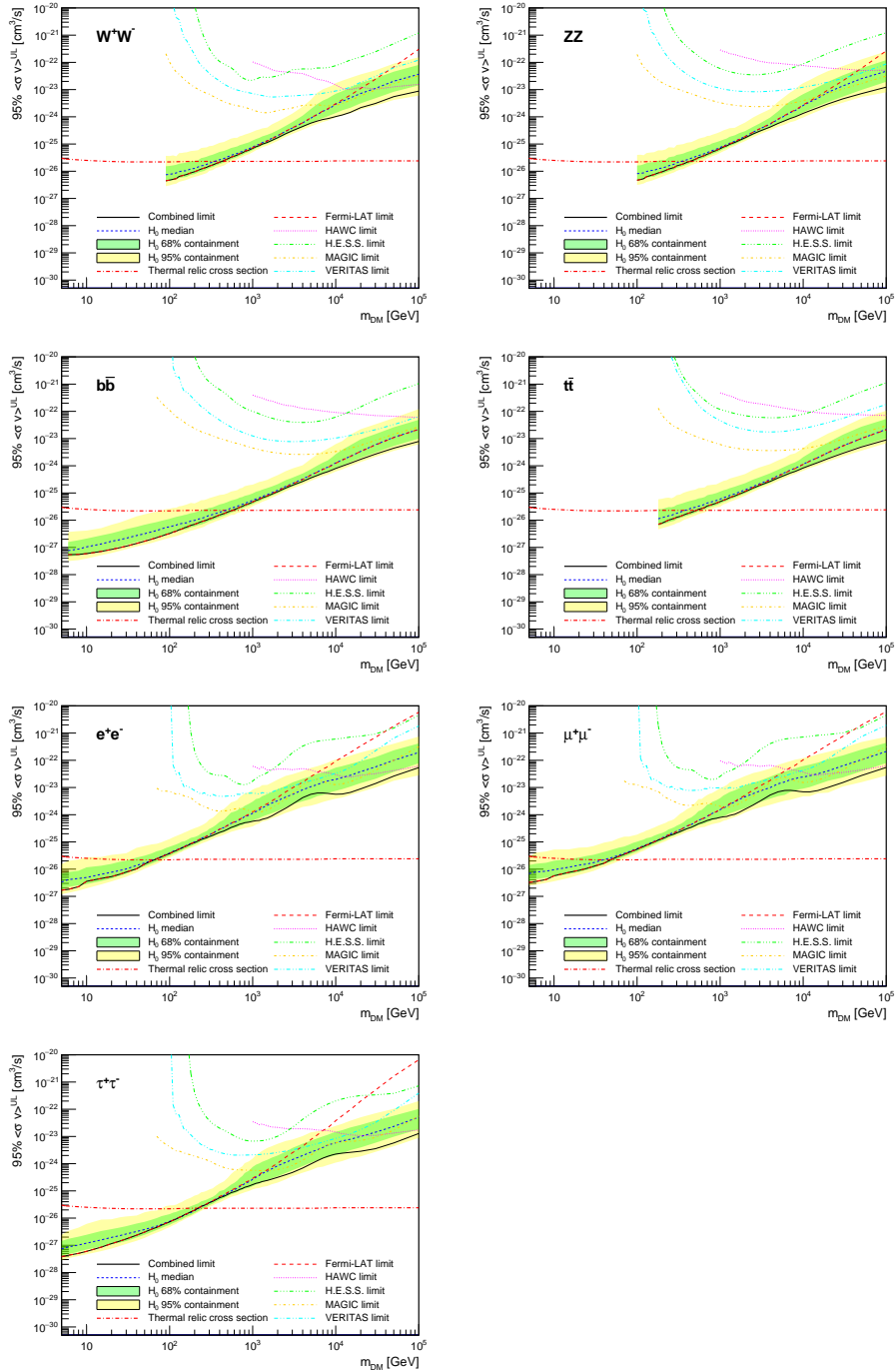


Figure 7.8 Same as Fig. 7.7, using the set of J factors from Ref. [46, 51] (\mathcal{B} set in Table 7.1).

sky for a specified annihilation channel. We calculated the change in gamma-ray counts for DM annihilation to primary $e\bar{e}$ for RA and Dec corresponding to Segue1 and Coma Berenices. These dSphs were chosen because they are the strongest contributors to the limit. $e\bar{e}$ was selected because it would have the largest number of high energy electrons. The effect was found to be on the order

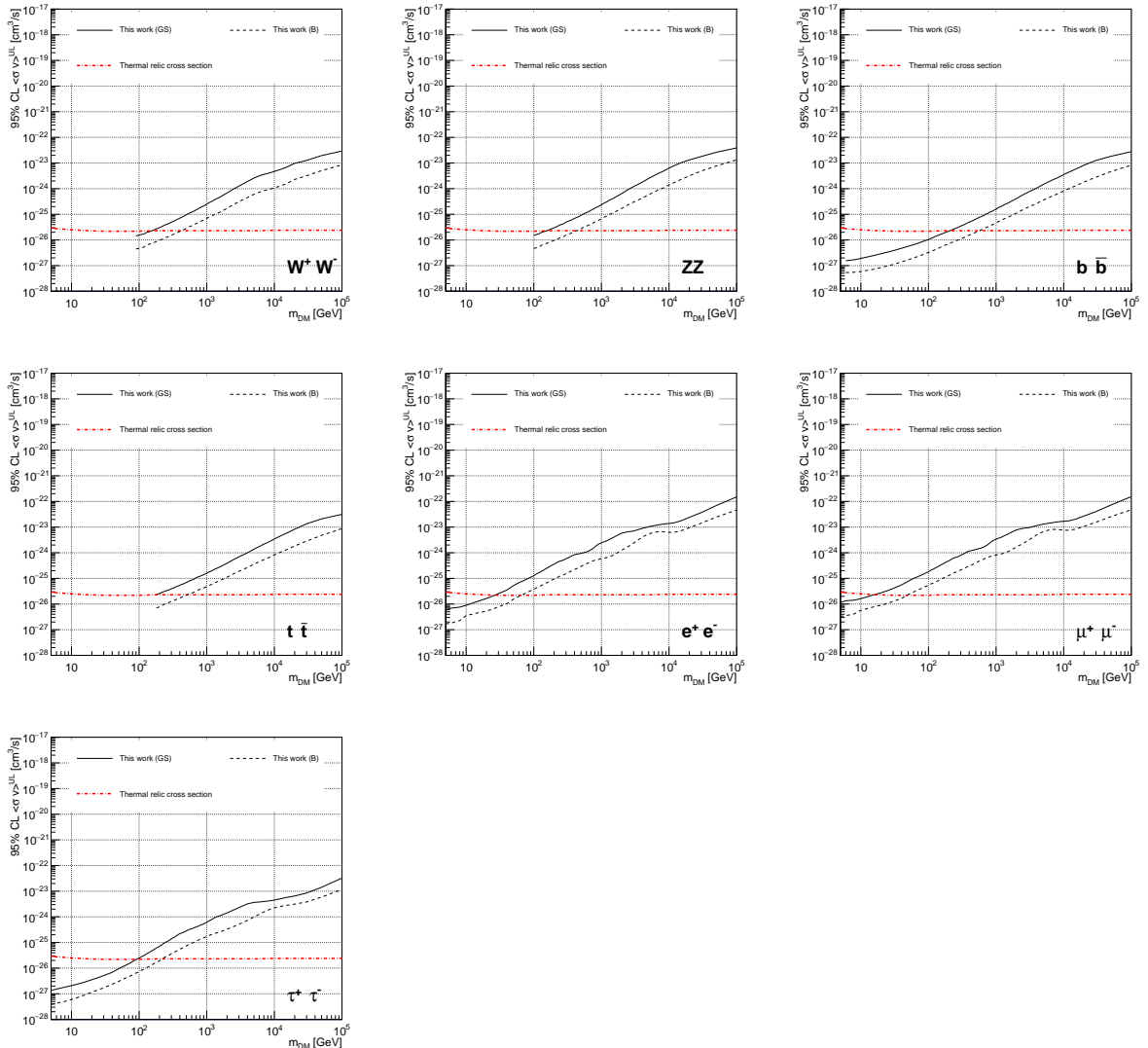


Figure 7.9 Comparisons of the combined limits at 95% confidence level for each of the eight annihilation channels when using the J factors from Ref. [47] (\mathcal{GS} set in Table 7.1), plain lines, and the J factor from Ref. [46, 51] (\mathcal{B} set in Table 7.1), dashed lines. The cross-section given by the thermal relic is also indicated [52].

866 of 10^{-7} on the gamma-ray spectrum. As a result, this systematic is not considered in our analysis.

867 7.6.2 Point Source Versus Extended Source Limits

868 The previous DM search toward dSph approximated the dSphs as point sources [45]. In
 869 this analysis, the dSphs are implemented as extended with J-factor distributions following those
 870 produced by [47]. The resolution of the cited map is much finer than HAWC's angular resolution.
 871 The vast majority of the J-factor distribution is represented on the central HAWC pixel of the dSph

872 spatial map. However, the neighboring 8 pixels are not negligible and contribute to our limit.

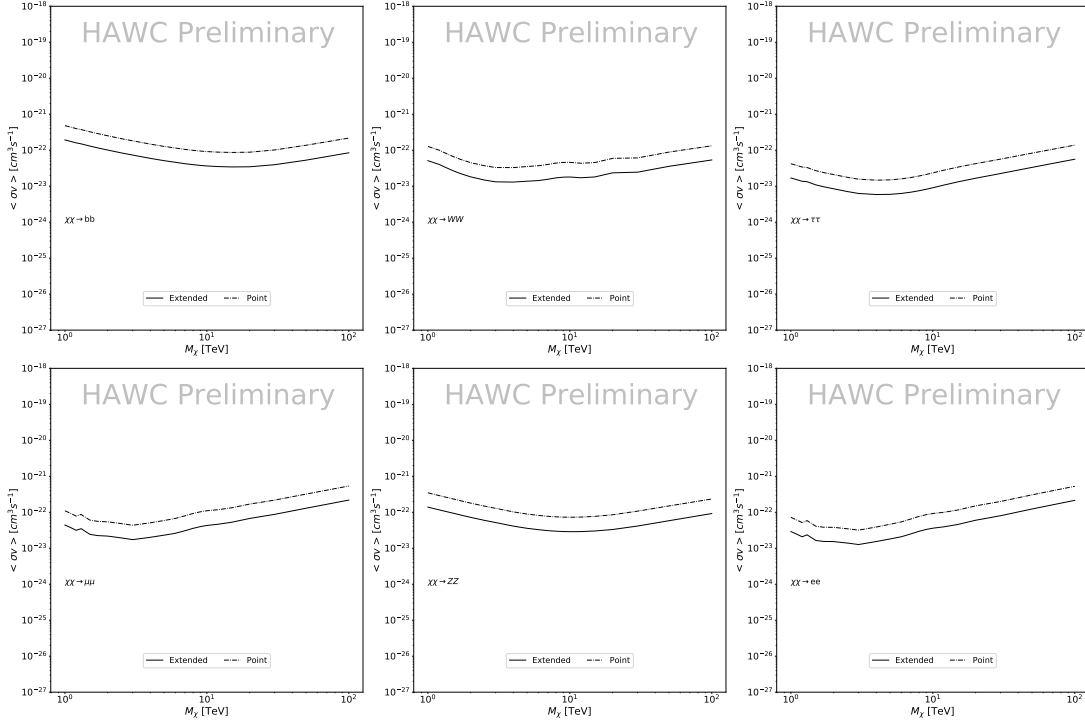


Figure 7.10 Comparisons of the combined limits at 95% confidence level for a point source analysis and extended source using [47] \mathcal{GS} J-factor distributions and PPPC [43] annihilation spectra. Shown are the limits for Segue1 which will have the most significant impact on the combined limit. 6 of the 7 DM annihilation channels are shown. Solid lines are extended source studies. Dashed lines are point source studies. Overall, the extended source analysis improves the limit by a factor of 2.

873 Figure 7.10 shows a substantial improvement to the limit for Segue1. Fig. 7.11 however showed
 874 identical limits. These disparities are best explained by the relative difference in their J-Factors.
 875 Both dSphs pass almost overhead the HAWC detector, however Segue1 has the larger J-Factor
 876 between the two. Adjacent pixels to the central pixel will therefore contribute to the limits. This is
 877 the case for other dSph that are closer to overhead the HAWC detector.

878 Comparison plots for all sources and the combined limit can be found in the sandbox for the
 879 Glory Duck project.

880 7.6.3 Impact of Pointing Systematic

881 During the analysis it was discovered that reconstruction of gamma-rays. Slides describing this
 882 systematic can be found [here](#). Shown on the presentation is dependence on the pointing systematic

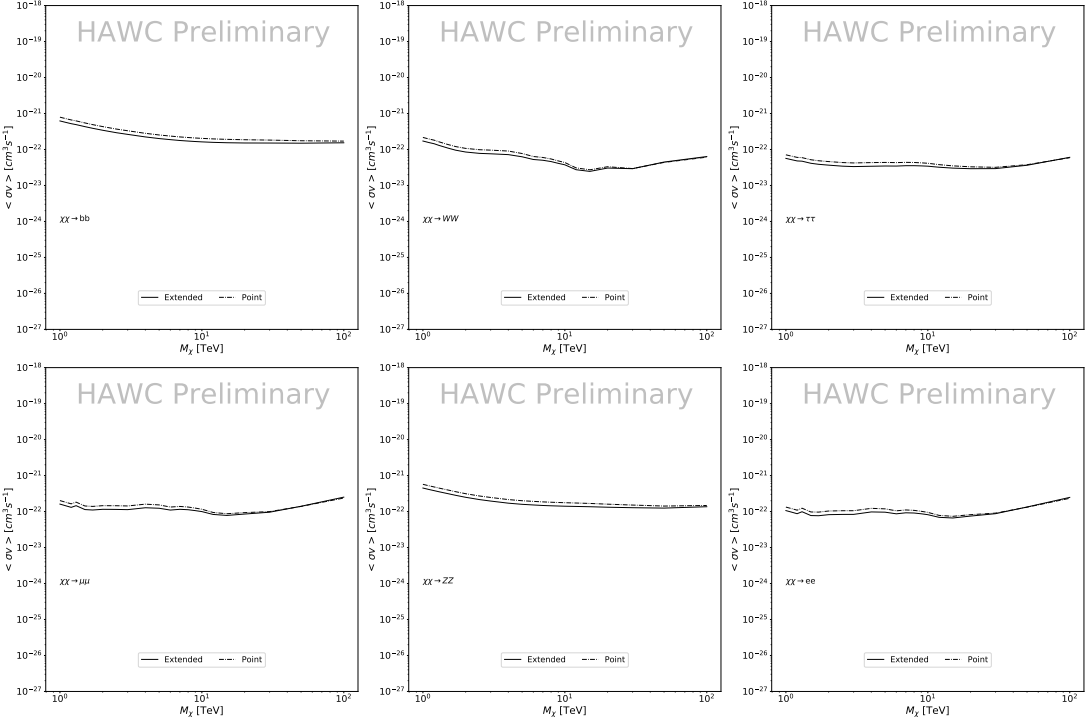


Figure 7.11 Same as Fig. 7.10 on Coma Berenices. This dSph also contributes significantly to the limit. The limits are identical in this case.

883 on declination. New spatial profiles were generated for every dSph and limits were computed for
 884 the adjusted declination.

885 Section 7.6.3 demonstrates the impact of this systematic for all DM annihilation channels
 886 studied by HAWC. The impact is a tiny improvement, yet mostly identical, to the combined limits.

887 7.7 J-factor distributions

888 7.7.1 Numerical integration of \mathcal{GS} maps

889 It was discovered well after the HAWC analysis was completed that the published tables from
 890 \mathcal{GS} [44] quoted median J -factors were computed in a non-trivial manner. The assumption myself
 891 and collaborators had was that the published tables represented the J -factor as a function of θ for
 892 the best global fit model on a per source basis. However, this is not the case. Instead, what is
 893 published are the best fit model for each dwarf that only considers stars up to the angular separation
 894 θ . Therefore, the model is changing for each value of θ for each dwarf. Yet, the introduced features
 895 from unique models at each θ are much smaller than the angular resolution of HAWC. It is not

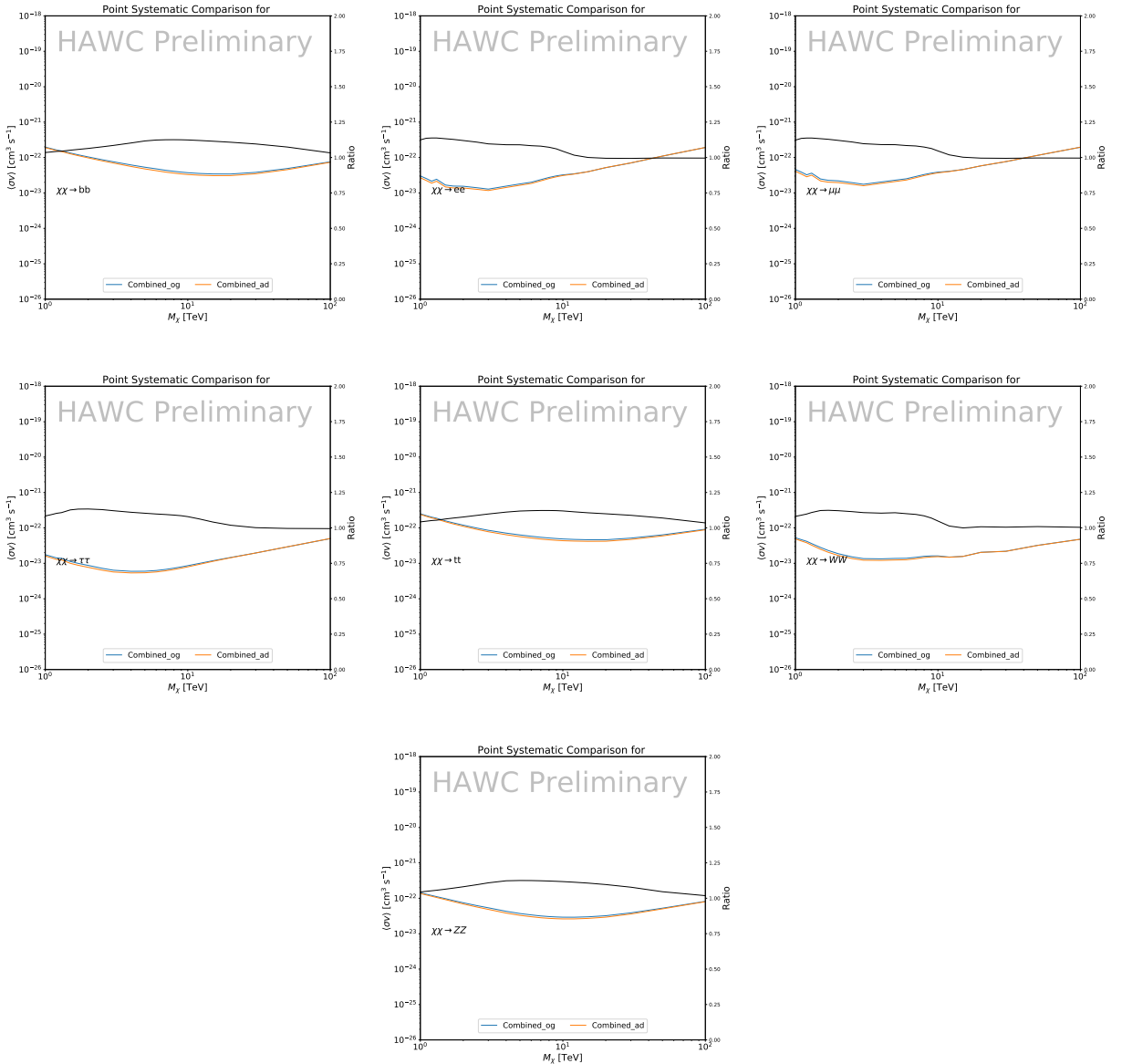


Figure 7.12 Comparison of combined limits when correcting for HAWC's pointing systematic. All DM annihilation channels are shown. The solid black line is the ratio between published limit to the declination corrected limit. The blue solid line or "Combined_og" represented the limits computed for Glory Duck. The solid orange line or "Combined_ad" represented the limits computed after correcting for the pointing systematic.

896 expected for these effects to impact the limits and TS greatly as a result.
 897 Median J -factor model profiles were provided by the authors. New maps were generated
 898 and analyzed for Segue1 and Coma Berenices. Figure 7.13 shows the differential between maps
 899 generated with the method from Section 7.7.1 and from the authors of [44]. These maps were

900 reanalyzed for all SM DM annihilation channels. Upper limits for these channels are shown in
901 Figure 7.14

902 From Figure 7.14, we can see that the impact of these model difference was no substantial.
903 The observed impact was a fractional effect which is much smaller than the impact from selecting
904 another DM spatial distribution model as was shown in Figure 7.9.

905 7.7.2 \mathcal{GS} versus \mathcal{B} spatial models

906 We show in this appendix a comparison between the J -factors computed by Geringer-Sameth
907 *et al.* [47] (the \mathcal{GS} set) and the ones computed by Bonnivard *et al.* [46, 51] (the \mathcal{B} set). The
908 \mathcal{GS} J -factors are computed through a Jeans analysis of the kinematic stellar data of the selected
909 dSphs, assuming a dynamic equilibrium and a spherical symmetry for the dSphs. They adopted
910 the generalized DM density distribution, known as Zhao-Hernquist, introduced by [53], carrying
911 three additional index parameters to describe the inner and outer slopes, and the break of the
912 density profile. Such a profile parametrization allows the reduction of the theoretical bias from
913 the choice of a specific radial dependency on the kinematic data. In other words, the increase of
914 free parameters with the use of the Zhao-Hernquist profile allows a better description of the mass
915 density distribution of dark matter.

916 In addition, a constant velocity anisotropy profile and a Plummer light profile [54] for the stellar
917 distribution were assumed. The velocity anisotropy profile depends on the radial and tangential
918 velocity dispersions. However, its determination remains challenging since only the line-of-sight
919 velocity dispersion can be derived from velocity measurements. Therefore, the parametrization of
920 the anisotropy profile is obtained from simulated halos (see [55] for more details). They provide the
921 values of the J -factors of regions extending to various angular radius up to the outermost member
922 star.

923 The \mathcal{B} J -factors were computed through a Jeans analysis taking into account the systematic
924 uncertainties induced by the DM profile parametrization, the radial velocity anisotropy profile, and
925 the triaxiality of the halo of the dwarf galaxies. They performed a more complete study of the dSph
926 kinematics and dynamics than \mathcal{GS} for the determination of the J -factor. Conservative values of the

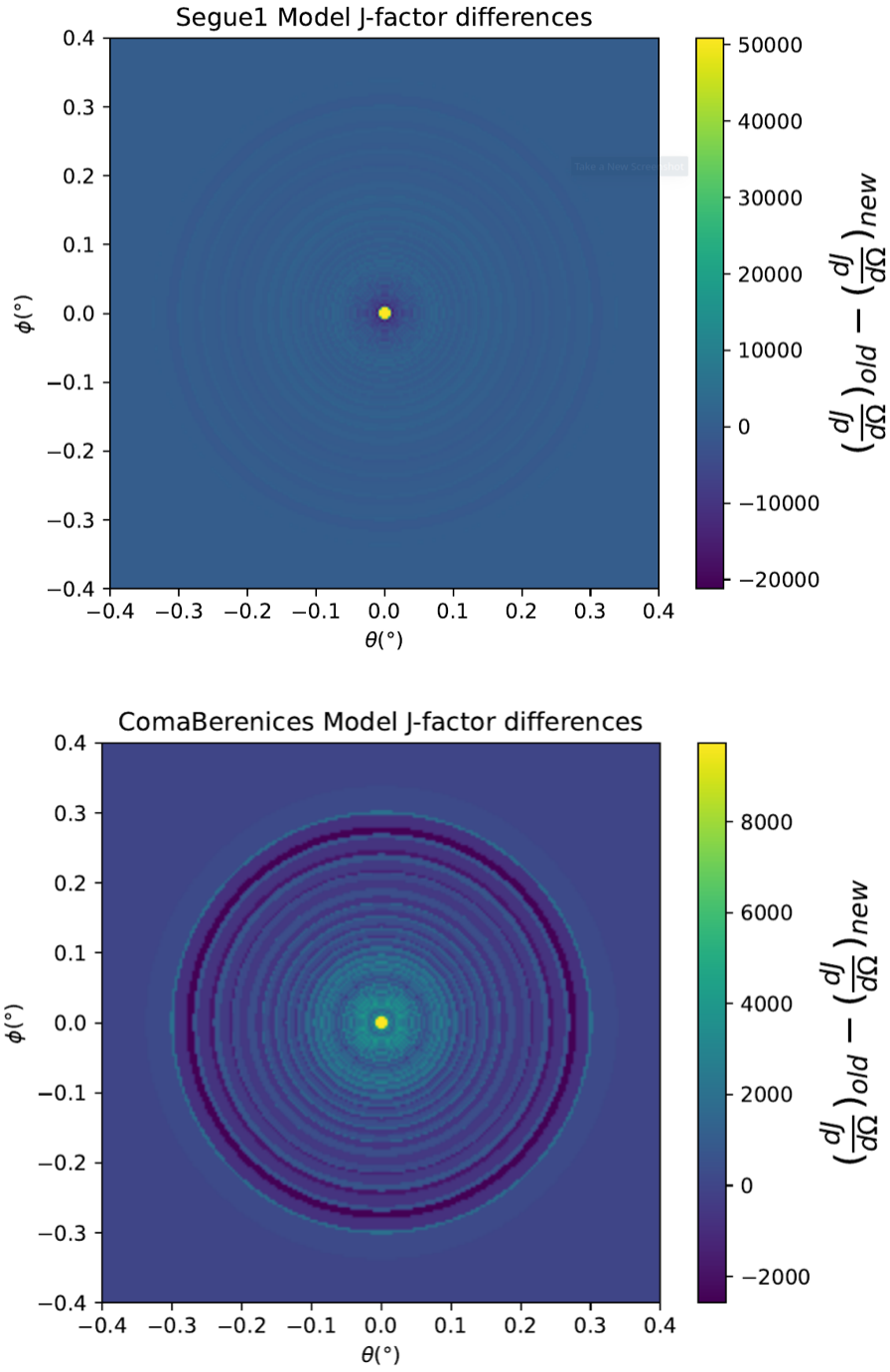


Figure 7.13 Differential map of dJ/Ω from model built in Section 7.7.1 and profiles provided directly from authors. (Top) Differential from Segue1. (bottom) Differential from Coma Berenices. Note that their scales are not the same. Segue1 shows the deepest discrepancies which is congruent with its large uncertainties. Both models show anuli where unique models become apparent.

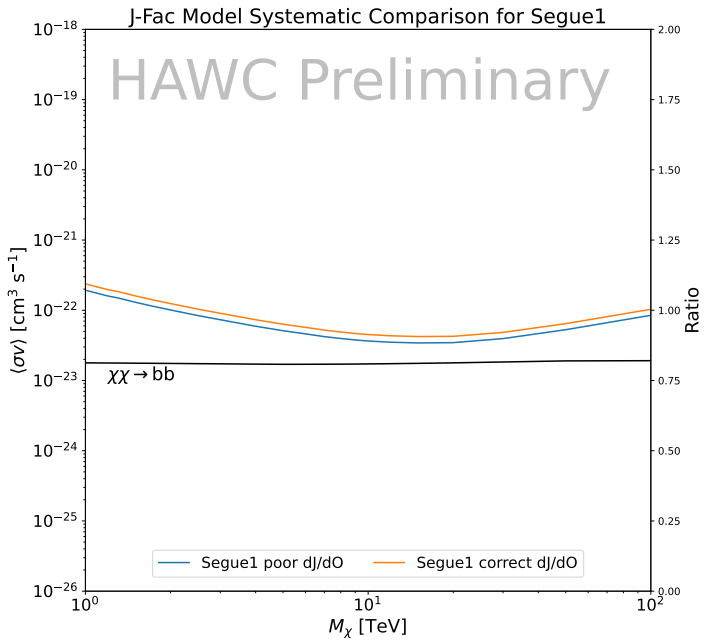
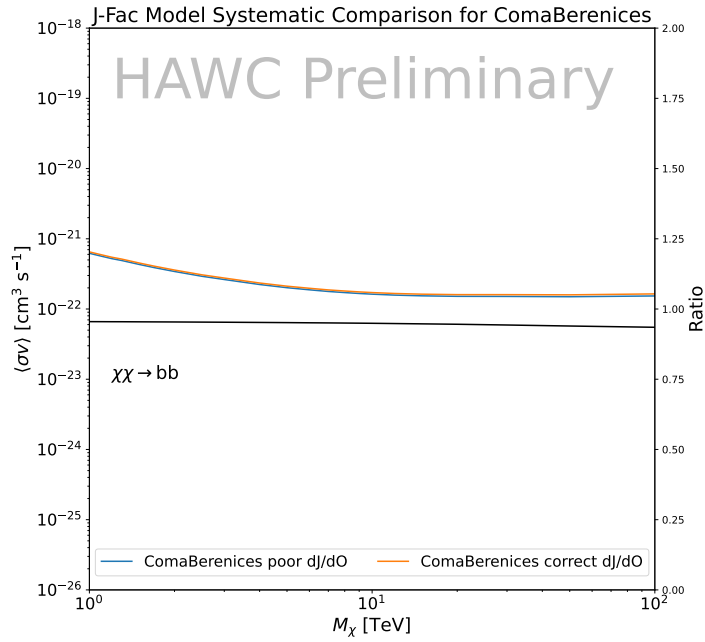


Figure 7.14 HAWC limits for Coma Berenices (top) and Segue1 (bottom) for two different map sets. Blue lines are limits calculated on maps with poor model representation. Orange lines are limits calculated on spatial profiles provided by the authors of [44]. Black line is the ratio of the poor spatial model limits to the corrected spatial models. The left y-axis measures $\langle \sigma v \rangle$ for the blue and orange lines. The right y-axis measures the ratio and is unitless.

927 J -factors where obtained using an Einasto DM density profile [56], a realistic anisotropy profile
928 known as the Baes & Van Hese profile [57] which takes into account that the inner regions can be
929 significantly non-isotropic, and a Zhao-Hernquist light profile [53].

930 For both sets, J -factor values are provided for all dSphs as a function of the radius of the
931 integration region [47, 46, 51]. Table 7.1 shows the heliocentric distance and Galactic coordinates
932 of the twenty dSphs, together with the two sets of J -factor values integrated up to the outermost
933 observed star for \mathcal{GS} and the tidal radius for \mathcal{B} . Both J -factor sets were derived through a Jeans
934 analysis based on the same kinematic data, except for Draco where the measurements of [58] have
935 been adopted in the computation of the \mathcal{B} value. The computations for producing the \mathcal{GS} and \mathcal{B}
936 samples differ in the choice of the DM density, velocity anisotropy, and light profiles, for which the
937 set \mathcal{B} takes into account some sources of systematic uncertainties.

938 Figure 7.15 and Figure 7.16 show the comparisons for the J -factor versus the angular radius
939 for each of the 20 dSphs used in this study. The uncertainties provided by the authors are also
940 indicated in the figures. For the \mathcal{GS} set, the computation stops at the angular radius corresponding
941 to the outermost observed star, while for the \mathcal{B} set, the computation stops at the angular radius
942 corresponding to the tidal radius.

943 7.8 Discussion and Conclusions

944 In this multi-instrument analysis, we have used observations of 20 dSphs from the gamma-ray
945 telescopes Fermi-LAT, H.E.S.S., MAGIC, VERITAS, and HAWC to perform a collective DM
946 search annihilation signals. The data were combined across sources and detectors to significantly
947 increase the sensitivity of the search. We have observed no significant deviation from the null, no
948 DM, hypothesis, and so present our results in terms of upper limits on the annihilation cross section
949 for seven potential DM annihilation channels.

950 Fermi-LAT brings the most stringent constraints for continuum channels below approximately
951 1 TeV. the remaining detectors dominate at higher energies. Overall, for multi-TeV DM mass,
952 the combined DM constraints from all five telescopes are 2-3 times stronger than any individual
953 telescope for multi-TeV DM.

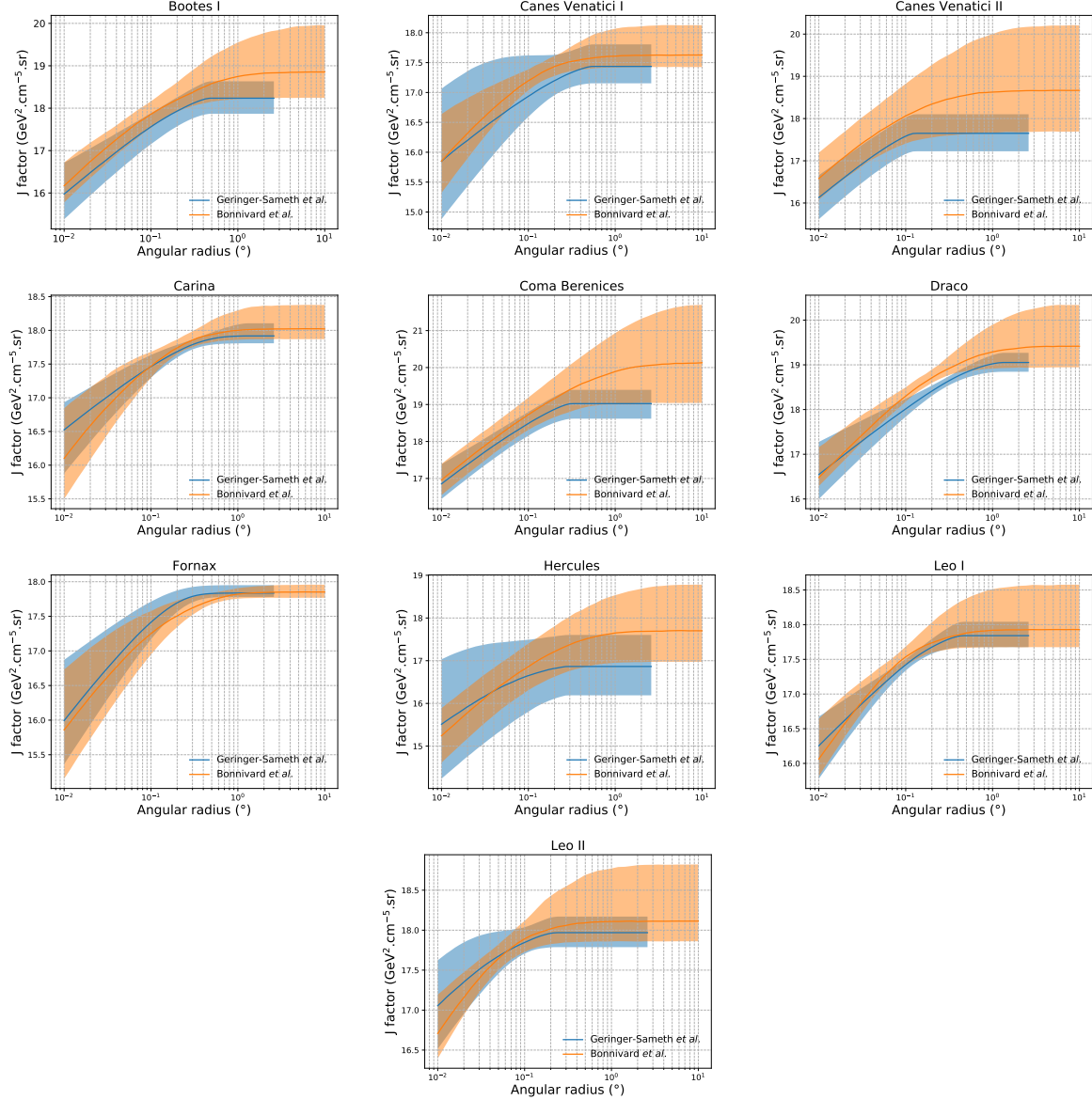


Figure 7.15 Comparisons between the J -factors versus the angular radius for the computation of J factors from Ref. [47] (\mathcal{GS} set in Table 7.1) in blue and for the computation from Ref. [46, 51] (\mathcal{B} set in Tab. 7.1) in orange. The solid lines represent the central value of the J -factors while the shaded regions correspond to the 1σ standard deviation.

954 Derived from observations of many dSphs, our results produce robust limits given the DM
 955 content of the dSphs is relatively well constrained. The obtained limits span the largest mass
 956 range of any WIMP DM search. Our combined analysis improves the sensitivity over previously
 957 published results from each detectors which produces the most stringent limits on DM annihilation
 958 from dSphs. These results are based on deep exposures of the most promising known dSphs with

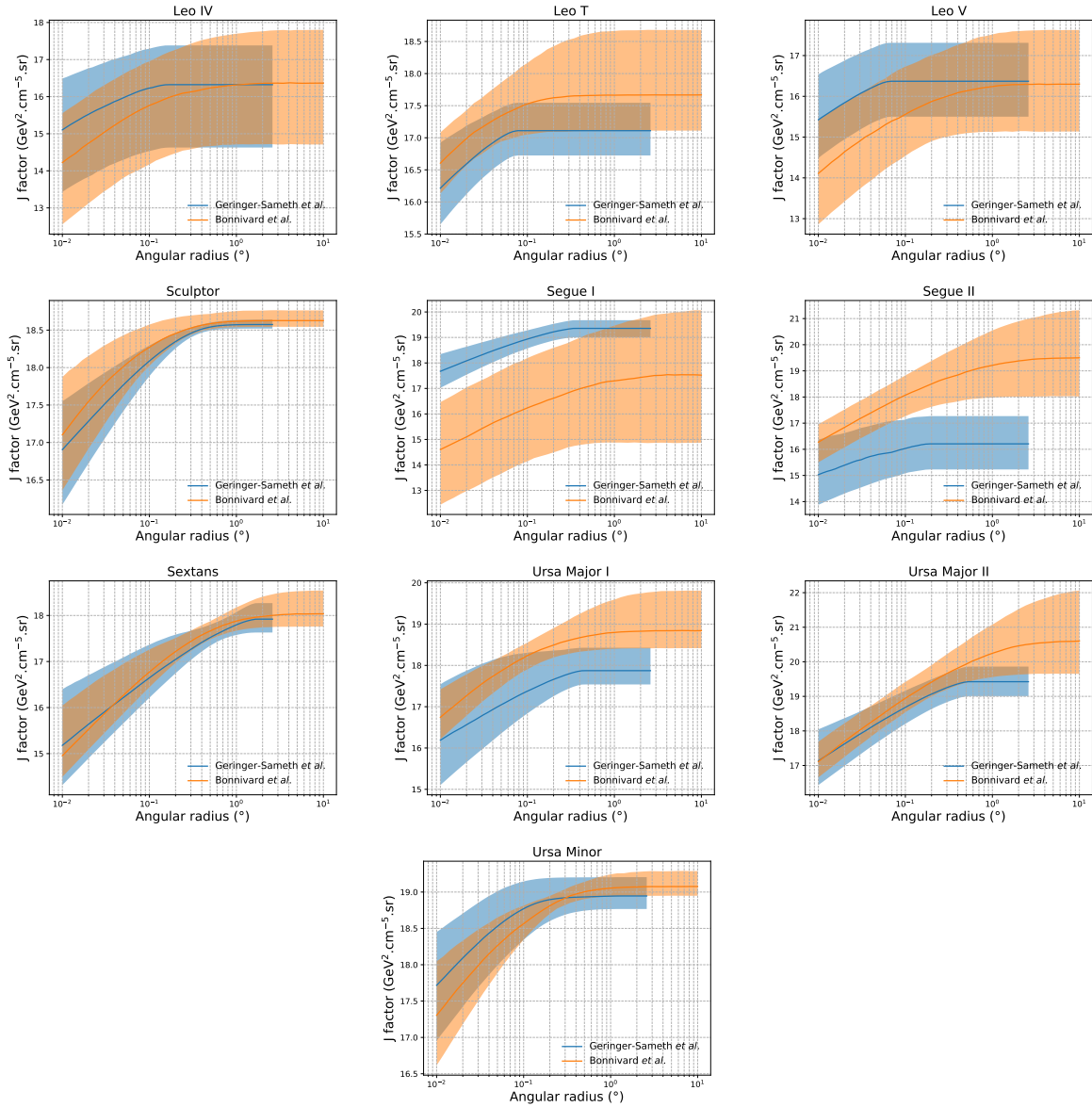


Figure 7.16 Comparisons between the J -factors versus the angular radius for the computation of J factors from Ref. [47] (\mathcal{GS} set in Tab. 7.1) in blue and for the computation from Ref. [46, 51] (\mathcal{B} set in Tab. 7.1) in orange. The solid lines represent the central value of the J -factors while the shaded regions correspond to the 1σ standard deviation.

959 the currently most sensitive gamma-ray instruments. Therefore, our results constitute a legacy of
 960 a generation of gamma-ray instruments on WIMP DM searches towards dSphs. Our results will
 961 remain the reference in the field until a new generation of more sensitive gamma-ray instruments
 962 begin operations, or until new dSphs with higher J -factors are discovered.

963 This analysis serves as a proof of concept for future multi-instrument and multi-messenger

964 combination analyses. With this collaborative effort, we have managed to sample over four orders
965 in magnitude in gamma-ray energies with distinct observational techniques. Determining the nature
966 of DM continues to be an elusive and difficult problem. Larger datasets with diverse measurement
967 techniques could be essential to tackling the DM problem. A future collaboration using similar
968 techniques as the ones described in this paper could grow even beyond gamma rays. The models we
969 used for this study include annihilation channels with neutrinos in the final state. Advanced studies
970 could aim to merge our results with those from neutrino observatories with large data sets. Efforts
971 are already underway to add data from the IceCube, ANTARES, and KM3NeT observatories to
972 these gamma-ray results.

973 From this work, a selection of the best candidates for observations, according to the latest
974 knowledge on stellar dynamics and modelling techniques for the derivation of the J -factors on the
975 potential dSphs targets, is highly desirable at the time that new experiments are starting their dark
976 matter programmes using dSphs. Given the systematic uncertainty inherent to the derivation of
977 the J -factors, an informed observational strategy would be to select both objects with the highest
978 J -factors that could lead to DM signal detection, and objects with robust J -factor predictions, i.e.
979 with kinematic measurements on many bright stars, which would strengthen the DM interpretation
980 reliability of the observation outcome.

981 This analysis combines data from multiple telescopes to produce strong constraints on astro-
982 physical objects. From this perspective, these methods can be applied beyond just DM searches.
983 Almost every astrophysical study can benefit from multi-telescope, multi-wavelength gamma-ray
984 studies. We have enabled these telescopes to study the cosmos with greater precision and detail.
985 Many astrophysical searches can benefit from multi-instrument gamma-ray studies, for which our
986 analysis lays the foundation.

CHAPTER 8

NU DUCK

987

CHAPTER 9

MULTITHREADING HAWC ANALYSES FOR DARK MATTER SEARCHES

APPENDIX A**MULTI-EXPERIMENT SUPPLEMENTARY FIGURES**

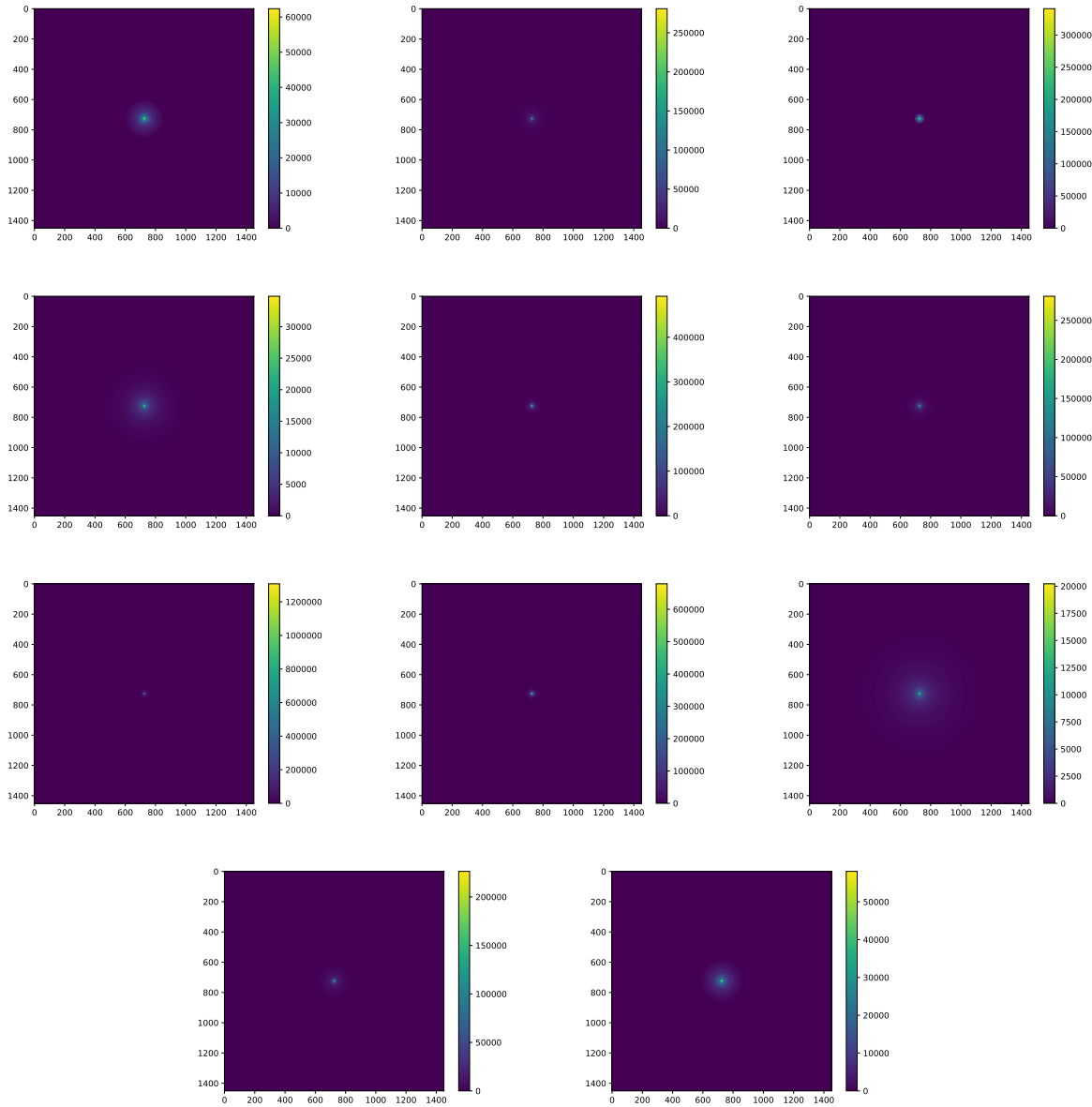


Figure A.1 Sister figure to Figure 7.3. Sources in the first row from left to right: Bootes I, Canes Venatici I, II. In second row: Draco, Hercules, Leo I. In the first row: Leo II, Leo IV, Sextans. In the final row: Ursa Major I, Ursa Major II.

BIBLIOGRAPHY

- 991 [1] Anne M. Green. “Dark matter in astrophysics/cosmology”. In: *SciPost Phys. Lect.*
 992 *Notes* (2022), p. 37. doi: [10.21468/SciPostPhysLectNotes.37](https://doi.org/10.21468/SciPostPhysLectNotes.37). URL: <https://scipost.org/10.21468/SciPostPhysLectNotes.37>.
- 994 [2] Bing-Lin Young. “A survey of dark matter and related topics in cosmology”. In: *Frontiers*
 995 *of Physics* 12 (Oct. 2016). doi: <https://doi.org/10.1007/s11467-016-0583-4>.
 996 URL: <https://doi.org/10.1007/s11467-016-0583-4>.
- 997 [3] Gianfranco Bertone, Dan Hooper, and Joseph Silk. “Particle dark matter: evidence,
 998 candidates and constraints”. In: *Physics Reports* 405.5 (2005), pp. 279–390. ISSN:
 999 0370-1573. doi: <https://doi.org/10.1016/j.physrep.2004.08.031>. URL:
 1000 <https://www.sciencedirect.com/science/article/pii/S0370157304003515>.
- 1001 [4] Gianfranco Bertone and Dan Hooper. “History of dark matter”. In: *Rev. Mod. Phys.*
 1002 90 (4 Aug. 2018), p. 045002. doi: [10.1103/RevModPhys.90.045002](https://doi.org/10.1103/RevModPhys.90.045002). URL: <https://link.aps.org/doi/10.1103/RevModPhys.90.045002>.
- 1004 [5] Fritz Zwicky. “The Redshift of Extragalactic Nebulae”. In: *Helvetica Physica Acta* 6.
 1005 (1933), pp. 110–127. doi: [10.5169/seals-110267](https://doi.org/10.5169/seals-110267).
- 1006 [6] Vera C. Rubin and Jr. Ford W. Kent. “Rotation of the Andromeda Nebula from a
 1007 Spectroscopic Survey of Emission Regions”. In: *ApJ* 159 (Feb. 1970), p. 379. doi:
 1008 [10.1086/150317](https://doi.org/10.1086/150317).
- 1009 [7] K. G. Begeman, A. H. Broeils, and R. H. Sanders. “Extended rotation curves of spiral galax-
 1010 ies: dark haloes and modified dynamics”. In: *Monthly Notices of the Royal Astronomical So-*
 1011 *ciety* 249.3 (Apr. 1991), pp. 523–537. ISSN: 0035-8711. doi: [10.1093/mnras/249.3.523](https://doi.org/10.1093/mnras/249.3.523).
 1012 eprint: <https://academic.oup.com/mnras/article-pdf/249/3/523/18160929/mnras249-0523.pdf>. URL: <https://doi.org/10.1093/mnras/249.3.523>.
- 1014 [8] *Different types of gravitational lenses*. website. Feb. 2004. URL: <https://esahubble.org/images/heic0404b/>.
- 1016 [9] Douglas Clowe et al. “A Direct Empirical Proof of the Existence of Dark Matter”. In: *apjl*
 1017 648.2 (Sept. 2006), pp. L109–L113. doi: [10.1086/508162](https://doi.org/10.1086/508162). arXiv: [astro-ph/0608407](https://arxiv.org/abs/astro-ph/0608407)
 1018 [[astro-ph](https://arxiv.org/abs/astro-ph/0608407)].
- 1019 [10] Planck Collaboration and N. et. al. Aghanim. “Planck 2018 results I. Overview and the
 1020 cosmological legacy of Planck”. In: *A&A* 641 (2020). doi: [10.1051/0004-6361/201833880](https://doi.org/10.1051/0004-6361/201833880). URL: <https://doi.org/10.1051/0004-6361/201833880>.
- 1022 [11] Wayne Hu. *Matter Density Animation*. web. 2024. URL: <http://background.uchicago.edu/~whu/animbut/anim2.html>.

- 1024 [12] Wenlong Yuan et al. “A First Look at Cepheids in a Type Ia Supernova Host with JWST”. in:
1025 *The Astrophysical Journal Letters* 940.1 (Nov. 2022). doi: [10.3847/2041-8213/ac9b27](https://doi.org/10.3847/2041-8213/ac9b27).
1026 URL: <https://dx.doi.org/10.3847/2041-8213/ac9b27>.
- 1027 [13] Wendy L. Freedman. “Measurements of the Hubble Constant: Tensions in Perspective”. In:
1028 *The Astrophysical Journal* 919.1 (Sept. 2021), p. 16. doi: [10.3847/1538-4357/ac0e95](https://doi.org/10.3847/1538-4357/ac0e95).
1029 URL: <https://dx.doi.org/10.3847/1538-4357/ac0e95>.
- 1030 [14] Jodi Cooley. “Dark Matter direct detection of classical WIMPs”. In: *SciPost Phys. Lect.*
1031 *Notes* (2022), p. 55. doi: [10.21468/SciPostPhysLectNotes.55](https://doi.org/10.21468/SciPostPhysLectNotes.55). URL: <https://scipost.org/10.21468/SciPostPhysLectNotes.55>.
- 1033 [15] “Search for new phenomena in events with an energetic jet and missing transverse momentum
1034 in pp collisions at $\sqrt{s} = 13$ TeV with the ATLAS detector”. In: *Phys. Rev. D* 103
1035 (11 July 2021), p. 112006. doi: [10.1103/PhysRevD.103.112006](https://doi.org/10.1103/PhysRevD.103.112006). URL: <https://link.aps.org/doi/10.1103/PhysRevD.103.112006>.
- 1037 [16] *Jetting into the dark side: a precision search for dark matter*. website. July 2020. URL:
1038 <https://atlas.cern/updates/briefing/precision-search-dark-matter>.
- 1039 [17] Celine Armand et. al. “Combined dark matter searches towards dwarf spheroidal galaxies
1040 with Fermi-LAT, HAWC, H.E.S.S., MAGIC, and VERITAS”. in: *Proceedings of Science*.
1041 Vol. 395. Mar. 2022. doi: <https://doi.org/10.22323/1.395.0528>.
- 1042 [18] Tracy R. Slatyer. “Les Houches Lectures on Indirect Detection of Dark Matter”. In: *SciPost*
1043 *Phys. Lect. Notes* (2022), p. 53. doi: [10.21468/SciPostPhysLectNotes.53](https://doi.org/10.21468/SciPostPhysLectNotes.53). URL:
1044 <https://scipost.org/10.21468/SciPostPhysLectNotes.53>.
- 1045 [19] Christian W Bauer, Nicholas L. Rodd, and Bryan R. Webber. “Dark matter spectra from
1046 the electroweak to the Planck scale”. In: *Journal of High Energy Physics* 2021.1029-8479
1047 (June 2021). doi: [https://doi.org/10.1007/JHEP06\(2021\)121](https://doi.org/10.1007/JHEP06(2021)121).
- 1048 [20] Riccardo Catena and Piero Ullio. “A novel determination of the local dark matter density”.
1049 In: *Journal of Cosmology and Astroparticle Physics* 2010.08 (Aug. 2010), p. 004. doi:
1050 [10.1088/1475-7516/2010/08/004](https://doi.org/10.1088/1475-7516/2010/08/004). URL: <https://dx.doi.org/10.1088/1475-7516/2010/08/004>.
- 1052 [21] B. P. Abbott et al. “Observation of Gravitational Waves from a Binary Black Hole Merger”.
1053 In: *Phys. Rev. Lett.* 116 (6 Feb. 2016), p. 061102. doi: [10.1103/PhysRevLett.116.061102](https://doi.org/10.1103/PhysRevLett.116.061102). URL: <https://link.aps.org/doi/10.1103/PhysRevLett.116.061102>.
- 1055 [22] R. Abbasi et. al. “Observation of high-energy neutrinos from the Galactic plane”. In: *Science*
1056 380.6652 (June 2023), pp. 1338–1343.
- 1057 [23] NASA Goddard Space Flight Center. *Fermi’s 12-year view of the gamma-ray sky*. website.

- 1058 2022. URL: <https://svs.gsfc.nasa.gov/14090>.
- 1059 [24] Marco Cirelli et al. “PPPC 4 DM ID: a poor particle physicist cookbook for dark matter
1060 indirect detection”. In: *Journal of Cosmology and Astroparticle Physics* 2011.03 (Mar.
1061 2011), p. 051. doi: [10.1088/1475-7516/2011/03/051](https://doi.org/10.1088/1475-7516/2011/03/051). URL: <https://dx.doi.org/10.1088/1475-7516/2011/03/051>.
- 1063 [25] W. B. Atwood et al. “The Large Area Telescope on the Fermi Gamma-Ray Space Telescope
1064 Mission”. In: *apj* 697.2 (June 2009), pp. 1071–1102. doi: [10.1088/0004-637X/697/2/1071](https://doi.org/10.1088/0004-637X/697/2/1071). arXiv: [0902.1089 \[astro-ph.IM\]](https://arxiv.org/abs/0902.1089).
- 1066 [26] M. Ackermann et al. “Searching for Dark Matter Annihilation from Milky Way Dwarf
1067 Spheroidal Galaxies with Six Years of Fermi Large Area Telescope Data”. In: *prl* 115.23,
1068 231301 (Dec. 2015), p. 231301. doi: [10.1103/PhysRevLett.115.231301](https://doi.org/10.1103/PhysRevLett.115.231301). arXiv:
1069 [1503.02641 \[astro-ph.HE\]](https://arxiv.org/abs/1503.02641).
- 1070 [27] Mattia Di Mauro, Martin Stref, and Francesca Calore. “Investigating the effect of Milky
1071 Way dwarf spheroidal galaxies extension on dark matter searches with Fermi-LAT data”.
1072 In: *Phys. Rev. D* 106 (12 Dec. 2022), p. 123032. doi: [10.1103/PhysRevD.106.123032](https://doi.org/10.1103/PhysRevD.106.123032).
1073 URL: <https://link.aps.org/doi/10.1103/PhysRevD.106.123032>.
- 1074 [28] F. et al. Aharonian. “Observations of the Crab Nebula with H.E.S.S.”. In: *Astron. Astrophys.*
1075 457 (2006), pp. 899–915. doi: [10.1051/0004-6361:20065351](https://doi.org/10.1051/0004-6361:20065351). arXiv: [astro-ph/0607333](https://arxiv.org/abs/astro-ph/0607333).
- 1077 [29] J. Albert et al. “VHE γ -Ray Observation of the Crab Nebula and its Pulsar with the MAGIC
1078 Telescope”. In: *The Astrophysical Journal* 674.2 (Feb. 2008), p. 1037. doi: [10.1086/525270](https://doi.org/10.1086/525270). URL: <https://dx.doi.org/10.1086/525270>.
- 1080 [30] N. Park. “Performance of the VERITAS experiment”. In: *Proceedings, 34th International
1081 Cosmic Ray Conference (ICRC2015): The Hague, The Netherlands, July, 30th July - 6th
1082 August*. Vol. 34. 2015, p. 771. arXiv: [1508.07070 \[astro-ph.IM\]](https://arxiv.org/abs/1508.07070).
- 1083 [31] A. Abramowski et al. “H.E.S.S. constraints on Dark Matter annihilations towards the Sculptor
1084 and Carina Dwarf Galaxies”. In: *Astropart. Phys.* 34 (2011), pp. 608–616. doi: [10.1016/j.astropartphys.2010.12.006](https://doi.org/10.1016/j.astropartphys.2010.12.006). arXiv: [1012.5602 \[astro-ph.HE\]](https://arxiv.org/abs/1012.5602).
- 1086 [32] A. Abramowski et al. “Search for dark matter annihilation signatures in H.E.S.S. observations
1087 of Dwarf Spheroidal Galaxies”. In: *Phys. Rev. D* 90 (2014), p. 112012. doi: [10.1103/PhysRevD.90.112012](https://doi.org/10.1103/PhysRevD.90.112012). arXiv: [1410.2589 \[astro-ph.HE\]](https://arxiv.org/abs/1410.2589).
- 1089 [33] H. Abdalla et al. “Searches for gamma-ray lines and ‘pure WIMP’ spectra from Dark
1090 Matter annihilations in dwarf galaxies with H.E.S.S”. in: *JCAP* 11 (2018), p. 037. doi:
1091 [10.1088/1475-7516/2018/11/037](https://doi.org/10.1088/1475-7516/2018/11/037). arXiv: [1810.00995 \[astro-ph.HE\]](https://arxiv.org/abs/1810.00995).

- 1092 [34] J. Aleksić et al. “Optimized dark matter searches in deep observations of Segue 1 with
1093 MAGIC”. in: *JCAP* 1402 (2014), p. 008. doi: [10.1088/1475-7516/2014/02/008](https://doi.org/10.1088/1475-7516/2014/02/008).
1094 arXiv: [1312.1535 \[hep-ph\]](https://arxiv.org/abs/1312.1535).
- 1095 [35] V.A. Acciari et al. “Combined searches for dark matter in dwarf spheroidal galaxies observed
1096 with the MAGIC telescopes, including new data from Coma Berenices and Draco”. In: *Physics of the Dark Universe* (2021), p. 100912. ISSN: 2212-6864. doi: <https://doi.org/10.1016/j.dark.2021.100912>. URL: <https://www.sciencedirect.com/science/article/pii/S2212686421001370>.
- 1100 [36] M. L. Ahnen et al. “Indirect dark matter searches in the dwarf satellite galaxy Ursa Major II
1101 with the MAGIC Telescopes”. In: *JCAP* 1803.03 (2018), p. 009. doi: [10.1088/1475-7516/2018/03/009](https://doi.org/10.1088/1475-7516/2018/03/009). arXiv: [1712.03095 \[astro-ph.HE\]](https://arxiv.org/abs/1712.03095).
- 1103 [37] S. et al. Archambault. “Dark matter constraints from a joint analysis of dwarf Spheroidal
1104 galaxy observations with VERITAS”. in: *prd* 95.8 (Apr. 2017). doi: [10.1103/PhysRevD.95.082001](https://doi.org/10.1103/PhysRevD.95.082001). arXiv: [1703.04937 \[astro-ph.HE\]](https://arxiv.org/abs/1703.04937).
- 1106 [38] Louise Oakes et al. “Combined Dark Matter searches towards dwarf spheroidal galaxies with
1107 Fermi-LAT, HAWC, HESS, MAGIC and VERITAS”. in: *Proceedings of Science*. 2019.
- 1108 [39] Celine Armand et al. on behalf of the Fermi-LAT, HAWC, HESS, MAGIC, VERITAS.
1109 “Combined Dark Matter searches towards dwarf spheroidal galaxies with Fermi-LAT,
1110 HAWC, HESS, MAGIC and VERITAS”. in: *Proceedings of Science*. 2021.
- 1111 [40] Daniel Kerszberg et al. on behalf of the Fermi-LAT, HAWC, HESS, MAGIC, and VER-
1112 TIAS collaborations. “Search for dark matter annihilation with a combined analysis of
1113 dwarf spheroidal galaxies from Fermi-LAT, HAWC, H.E.S.S., MAGIC and VERITAS”. in:
1114 *Proceedings of Science*. 2023.
- 1115 [41] A. U. Abeysekara et al. “Observation of the Crab Nebula with the HAWC Gamma-Ray
1116 Observatory”. In: *The Astrophysical Journal* 843.1 (June 2017), p. 39. doi: [10.3847/1538-4357/aa7555](https://doi.org/10.3847/1538-4357/aa7555). URL: <https://doi.org/10.3847/1538-4357/aa7555>.
- 1118 [42] Giacomo Vianello et al. *The Multi-Mission Maximum Likelihood framework (3ML)*. 2015.
1119 arXiv: [1507.08343 \[astro-ph.HE\]](https://arxiv.org/abs/1507.08343).
- 1120 [43] Marco Cirelli et al. “PPPC 4 DM ID: a poor particle physicist cookbook for dark matter
1121 indirect detection”. In: *Journal of Cosmology and Astroparticle Physics* 2011.03 (Mar.
1122 2011). ISSN: 1475-7516. doi: [10.1088/1475-7516/2011/03/051](https://doi.org/10.1088/1475-7516/2011/03/051). URL: <http://dx.doi.org/10.1088/1475-7516/2011/03/051>.
- 1124 [44] Alex Geringer-Sameth, Savvas M. Koushiappas, and Matthew Walker. “DWARF GALAXY
1125 ANNIHILATION AND DECAY EMISSION PROFILES FOR DARK MATTER EXPERI-
1126 MENTS”. in: *The Astrophysical Journal* 801.2 (Mar. 2015), p. 74. ISSN: 1538-4357. doi:

- 1127 10.1088/0004-637X/801/2/74. URL: <http://dx.doi.org/10.1088/0004-637X/80>
1128 1/2/74.
- 1129 [45] A. Albert et al. “Dark Matter Limits from Dwarf Spheroidal Galaxies with the HAWC
1130 Gamma-Ray Observatory”. In: *The Astrophysical Journal* 853.2 (Feb. 2018), p. 154. ISSN:
1131 1538-4357. doi: [10.3847/1538-4357/aaa6d8](https://doi.org/10.3847/1538-4357/aaa6d8). URL: <http://dx.doi.org/10.3847/1538-4357/aaa6d8>.
- 1133 [46] V. Bonnivard et al. “Spherical Jeans analysis for dark matter indirect detection in dwarf
1134 spheroidal galaxies - Impact of physical parameters and triaxiality”. In: *Mon. Not. Roy.
1135 Astron. Soc.* 446 (2015), pp. 3002–3021. doi: [10.1093/mnras/stu2296](https://doi.org/10.1093/mnras/stu2296). arXiv:
1136 [1407.7822 \[astro-ph.HE\]](https://arxiv.org/abs/1407.7822).
- 1137 [47] Alex Geringer-Sameth and Matthew Koushiappas Savvas M. and Walker. “Dwarf galaxy
1138 annihilation and decay emission profiles for dark matter experiments”. In: *Astrophys.
1139 J.* 801.2 (2015), p. 74. doi: [10.1088/0004-637X/801/2/74](https://doi.org/10.1088/0004-637X/801/2/74). arXiv: [1408.0002](https://arxiv.org/abs/1408.0002)
1140 [astro-ph.CO].
- 1141 [48] M. Ackermann et al. “Searching for Dark Matter Annihilation from Milky Way Dwarf
1142 Spheroidal Galaxies with Six Years of Fermi Large Area Telescope Data”. In: *prl* 115.23,
1143 231301 (Dec. 2015), p. 231301. doi: [10.1103/PhysRevLett.115.231301](https://doi.org/10.1103/PhysRevLett.115.231301). arXiv:
1144 [1503.02641 \[astro-ph.HE\]](https://arxiv.org/abs/1503.02641).
- 1145 [49] A. et al. Albert. “Searching for Dark Matter Annihilation in Recently Discovered Milky Way
1146 Satellites with Fermi-LAT”. in: *Astrophys. J.* 834.2 (2017), p. 110. doi: [10.3847/1538-4](https://doi.org/10.3847/1538-4)
1147 [357/834/2/110](https://arxiv.org/abs/1611.03184). arXiv: [1611.03184 \[astro-ph.HE\]](https://arxiv.org/abs/1611.03184).
- 1148 [50] Mattia Di Mauro and Martin Wolfgang Winkler. “Multimessenger constraints on the dark
1149 matter interpretation of the Fermi-LAT Galactic Center excess”. In: *prd* 103.12, 123005
1150 (June 2021), p. 123005. doi: [10.1103/PhysRevD.103.123005](https://doi.org/10.1103/PhysRevD.103.123005). arXiv: [2101.11027](https://arxiv.org/abs/2101.11027)
1151 [astro-ph.HE].
- 1152 [51] V. Bonnivard et al. “Dark matter annihilation and decay in dwarf spheroidal galaxies: The
1153 classical and ultrafaint dSphs”. In: *Mon. Not. Roy. Astron. Soc.* 453.1 (2015), pp. 849–867.
1154 doi: [10.1093/mnras/stv1601](https://doi.org/10.1093/mnras/stv1601). arXiv: [1504.02048 \[astro-ph.HE\]](https://arxiv.org/abs/1504.02048).
- 1155 [52] Gianfranco Bertone, Dan Hooper, and Joseph Silk. “Particle dark matter: evidence, can-
1156 didates and constraints”. In: *Physics Reports* 405.5-6 (Jan. 2005), pp. 279–390. ISSN:
1157 0370-1573. doi: [10.1016/j.physrep.2004.08.031](https://doi.org/10.1016/j.physrep.2004.08.031). URL: <http://dx.doi.org/10.1016/j.physrep.2004.08.031>.
- 1159 [53] HongSheng Zhao. “Analytical models for galactic nuclei”. In: *Mon. Not. Roy. Astron. Soc.*
1160 278 (1996), pp. 488–496. doi: [10.1093/mnras/278.2.488](https://doi.org/10.1093/mnras/278.2.488). arXiv: [astro-ph/9509122](https://arxiv.org/abs/astro-ph/9509122)
1161 [astro-ph].

- 1162 [54] H. C. Plummer. “On the Problem of Distribution in Globular Star Clusters: (Plate 8.)”
1163 In: *Monthly Notices of the Royal Astronomical Society* 71.5 (Mar. 1911), pp. 460–470.
1164 ISSN: 0035-8711. doi: [10.1093/mnras/71.5.460](https://doi.org/10.1093/mnras/71.5.460). eprint: <https://academic.oup.com/mnras/article-pdf/71/5/460/2937497/mnras71-0460.pdf>. URL:
1165 <https://doi.org/10.1093/mnras/71.5.460>.
- 1167 [55] Daniel R. Hunter. “Derivation of the anisotropy profile, constraints on the local velocity
1168 dispersion, and implications for direct detection”. In: *JCAP* 02 (2014), p. 023. doi:
1169 [10.1088/1475-7516/2014/02/023](https://doi.org/10.1088/1475-7516/2014/02/023). arXiv: [1311.0256 \[astro-ph.CO\]](https://arxiv.org/abs/1311.0256).
- 1170 [56] Barun Kumar Dhar and Liliya L. R. Williams. “Surface mass density of the Einasto family
1171 of dark matter haloes: are they Sersic-like?” In: *Mon. Not. Roy. Astron. Soc.* (2010). doi:
1172 [10.1111/j.1365-2966.2010.16446.x](https://doi.org/10.1111/j.1365-2966.2010.16446.x).
- 1173 [57] M. Baes and E. Van Hese. “Dynamical models with a general anisotropy profile”. In: *Astron. Astrophys.* 471 (2007), p. 419. doi: [10.1051/0004-6361:20077672](https://doi.org/10.1051/0004-6361:20077672). arXiv:
1174 [0705.4109 \[astro-ph\]](https://arxiv.org/abs/0705.4109).
- 1176 [58] Matthew G. Walker, Edward W. Olszewski, and Mario Mateo. “Bayesian analysis of re-
1177 solved stellar spectra: application to MMT/Hectochelle observations of the Draco dwarf
1178 spheroidal”. In: *mnras* 448.3 (Apr. 2015), pp. 2717–2732. doi: [10.1093/mnras/stv099](https://doi.org/10.1093/mnras/stv099).
1179 arXiv: [1503.02589 \[astro-ph.GA\]](https://arxiv.org/abs/1503.02589).